Astronomy & Astrophysics

Pulsating red giant stars in eccentric binary systems discovered from *Kepler* space-based photometry

A sample study and the analysis of KIC 5006817

P. G. Beck[1], K. Hambleton[2,1], J. Vos[1], T. Kallinger[3], S. Bloemen[1], A. Tkachenko[1], R. A. García[4], R. H. Østensen[1],
C. Aerts[1,5], D. W. Kurtz[2], J. De Ridder[1], S. Hekker[6], K. Pavlovski[7], S. Mathur[8], K. De Smedt[1], A. Derekas[9],
E. Corsaro[1], B. Mosser[10], H. Van Winckel[1], D. Huber[11], P. Degroote[1], G. R. Davies[12], A. Prša[13], J. Debosscher[1],
Y. Elsworth[12], P. Nemeth[1], L. Siess[14], V. S. Schmid[1], P. I. Pápics[1], B. L. de Vries[1], A. J. van Marle[1],
P. Marcos-Arenal[1], and A. Lobel[15]

[1] Instituut voor Sterrenkunde, KU Leuven, 3001 Leuven, Belgium
  e-mail: paul.beck@ster.kuleuven.be
[2] Jeremiah Horrocks Institute, University of Central Lancashire, Preston PR1 2HE, UK
[3] Institut für Astronomie der Universität Wien, Türkenschanzstr. 17, 1180 Wien, Austria
[4] Laboratoire AIM, CEA/DSM-CNRS – Université Denis Diderot-IRFU/SAp, 91191 Gif-sur-Yvette Cedex, France
[5] Department of Astrophysics, IMAPP, University of Nijmegen, PO Box 9010, 6500 GL Nijmegen, The Netherlands
[6] Astronomical Institute Anton Pannekoek, University of Amsterdam, Science Park 904, 1098 XH Amsterdam, The Netherlands
[7] Department of Physics, Faculty of Science, University of Zagreb, 10000 Zagreb, Croatia
[8] Space Science Institute, 4750 Walnut street Suite #205, Boulder CO 80301, USA
[9] Konkoly Observ., Research Centre f. Astronomy and Earth Sciences, Hungarian Academy of Sciences, 1121 Budapest, Hungary
[10] LESIA, CNRS, Université Pierre et Marie Curie, Université Denis Diderot, Observatoire de Paris, 92195 Meudon Cedex, France
[11] NASA Ames Research Center, Moffett Field CA 94035, USA
[12] School of Physics and Astronomy, University of Birmingham, Edgebaston, Birmingham B13 2TT, UK
[13] Department of Astronomy and Astrophysics, Villanova University, 800 East Lancaster avenue, Villanova PA 19085, USA
[14] Institut d'Astronomie et d'Astrophysique, Univ. Libre de Bruxelles, CP226, boulevard du Triomphe, 1050 Brussels, Belgium
[15] Royal Observatory of Belgium, Ringlaan 3, 1180 Brussels, Belgium

ABSTRACT

Context. The unparalleled photometric data obtained by NASA's *Kepler* Space Telescope has led to improved understanding of red giant stars and binary stars. Seismology allows us to constrain the properties of red giants. In addition to eclipsing binaries, eccentric non-eclipsing binaries that exhibit ellipsoidal modulations have been detected with *Kepler*.
Aims. We aim to study the properties of eccentric binary systems containing a red giant star and to derive the parameters of the primary giant component.
Methods. We applied asteroseismic techniques to determine the masses and radii of the primary component of each system. For a selected target, light and radial velocity curve modelling techniques were applied to extract the parameters of the system and its primary component. Stellar evolution and its effects on the evolution of the binary system were studied from theoretical models.
Results. The paper presents the asteroseismic analysis of 18 pulsating red giants in eccentric binary systems, for which masses and radii were constrained. The orbital periods of these systems range from 20 to 440 days. The results of our ongoing radial velocity monitoring programme with the Hermes spectrograph reveal an eccentricity range of $e = 0.2$ to 0.76. As a case study we present a detailed analysis of KIC 5006817, whose rich oscillation spectrum allows for detailed seismic analysis. From seismology we constrain the rotational period of the envelope to be at least 165 d, which is roughly twice the orbital period. The stellar core rotates 13 times faster than the surface. From the spectrum and radial velocities we expect that the Doppler beaming signal should have a maximum amplitude of 300 ppm in the light curve. Fixing the mass and radius to the asteroseismically determined values, we find from our binary modelling a value of the gravity darkening exponent that is significantly larger than expected. Through binary modelling, we determine the mass of the secondary component to be $0.29 \pm 0.03\ M_\odot$.
Conclusions. For KIC 5006817 we exclude pseudo-synchronous rotation of the red giant with the orbit. The comparison of the results from seismology and modelling of the light curve shows a possible alignment of the rotational and orbital axis at the 2σ level. Red giant eccentric systems could be progenitors of cataclysmic variables and hot subdwarf B stars.

Key words. stars: solar-type – binaries: general – stars: rotation – Sun: oscillations – stars: individual: KIC5006817 – asteroseismology

1. Introduction

The NASA *Kepler* space telescope (Borucki et al. 2010) has been delivering unprecedented photometric data for more than 150 000 stars. These nearly continuous observations that now cover more than 1000 d have allowed major advances in our understanding of stellar structure of single stars and of multiple-star systems. The asteroseismic investigation of red giant stars has become one of *Kepler's* success stories.

Red giants are evolved stars that have ceased hydrogen burning in the core and left the main sequence. This late phase of stellar evolution splits into several episodes, which are associated
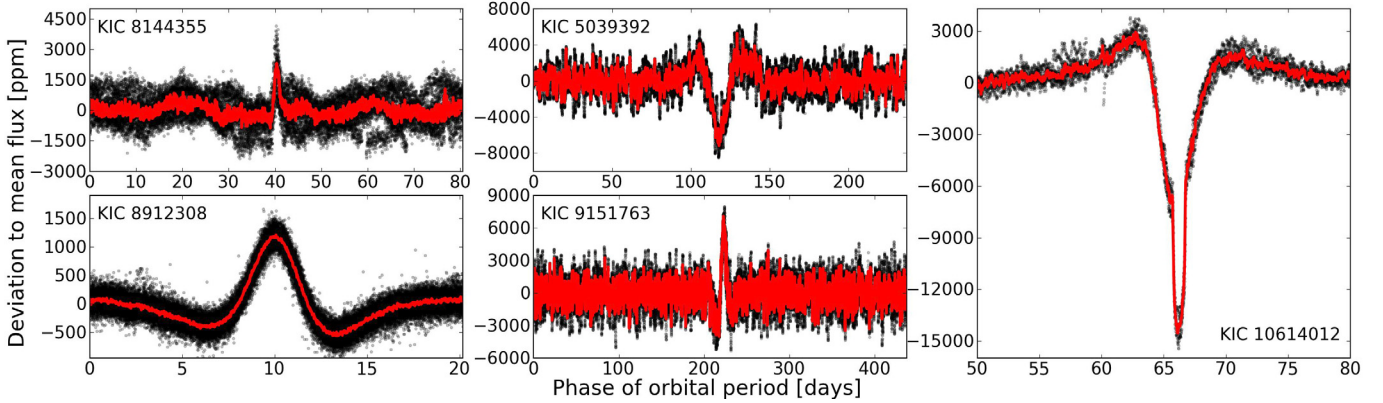
Fig. 1. Five examples of *Kepler* light curves of red giant heartbeat stars from our sample. Black dots and red line show the corrected and rebinned (30 min) light curves, respectively. KIC 8144355 is the star with the highest eccentricity, KIC 5039392 is the most luminous star, and KIC 9151763 is the star with the longest orbital period. The low-luminosity RGB star KIC 8912308 has the shortest orbital period in our sample. The *right panel* shows a zoom on the partial eclipse during the heartbeat event of KIC 10614012.

with subsequent modifications of the stellar structure. As the helium core contracts, the energy generation rate in the hydrogen-burning shell that surrounds the core increases the luminosity causing an increase in the stellar radius. The core's mass and density keep growing until the core is hot enough to ignite helium, as the helium settles from the burning hydrogen shell. For stars with birth masses below approximately 2.3 $M_\odot$, the helium core fusion starts with a helium flash in a series of off-centre thermal subflashes (e.g. Bildsten et al. 2012) that result in a thermal runaway. At this point the core expands by two orders of magnitude, reducing the temperature of the overlying hydrogen-burning shell. The luminosity of the star drops, the radius contracts and the red giant settles onto the horizontal branch, where metal-rich stars are concentrated in the red clump.

A large portion (in radius) of the red giant's envelope is convective, and oscillations are excited stochastically in a part of that envelope. These solar-like oscillations correspond to pressure modes (p modes), and their frequencies follow a characteristic comb-like pattern (Tassoul 1980). The mode amplitudes range from a few tens to a few hundred parts per million (ppm) in observed flux, or of the order of $10 \, \mathrm{m \, s^{-1}}$ or less in radial velocity (Frandsen et al. 2002; De Ridder et al. 2006), which is barely detectable from ground-based observations. In the era before high-precision photometric space missions, solar-like oscillations of red giants were only confirmed in a handful of bright stars from extensive single- and multisite campaigns of high-precision spectroscopy. Examples are ξ Hya (Frandsen et al. 2002), ε Oph (De Ridder et al. 2006), and η Ser (Hekker et al. 2006). Photometric measurements from space have substantially increased the number of red giants with detected oscillation signals. The detection of nonradial modes in a multitude of red giants observed with the CoRoT satellite was a major milestone towards an improved understanding of red giants, since it allowed for more sophisticated asteroseismic analyses (De Ridder et al. 2009).

Pressure modes have their largest amplitude in the convective envelope, while gravity modes (g modes) have their largest amplitude in the deep interior. At some stages of stellar evolution, p modes and g modes can couple and become a mixed mode. The firm identification of such mixed modes in *Kepler* and CoRoT data by Beck et al. (2011), Bedding et al. (2011), and Mosser et al. (2011a) extended the sensitivity of the seismic analysis towards the core regions of red giant stars (Dupret et al. 2009, and references therein). The analysis of mixed modes allows us to determine the evolutionary

state (Bedding et al. 2011; Mosser et al. 2011a) and constrain the core rotation of red giants (Beck et al. 2012; Deheuvels et al. 2012).

The seismology of red giants is largely built on scaling relations for pressure modes that have already been described by Kjeldsen & Bedding (1995). These relations have been applied in numerous papers since then (e.g. Kallinger et al. 2010b; Huber et al. 2011; Corsaro et al. 2013). Results from scaling relations have recently been compared with results of independent methods. Huber et al. (2012) found a good agreement within the observational uncertainties for evolved stars. From comparing results for the eclipsing binary KIC 8410637 from binary modelling and seismology, Frandsen et al. (2013) found an excellent agreement for the surface gravity. But, the masses determined by the two methods deviated slightly. Additionally, a large set of red giants in eclipsing binaries was recently reported by Gaulme et al. (2013) which will allow for new sample studies.

The *Kepler* mission has also recently discovered the existence of a new class of eccentric ellipsoidal binary stars for which the binary characteristics can be determined over the complete range of inclinations and as such are not limited to the narrow range of eclipsing systems. These so-called *Heartbeat* stars (Welsh et al. 2011; Thompson et al. 2012) are defined as eccentric, detached binary systems that undergo strong gravitational distortions and heating during periastron passage, which are clearly depicted in their light curves (e.g. Fig. 1). Kumar et al. (1995) developed a theory of such objects and demonstrated how the morphology of the light curve is defined by the eccentricity, argument of periastron and inclination. Furthermore, the amplitude of the periastron variation is determined by the periastron separation, masses and structure of the stellar components. Consequently, these parameters can in principle be gauged through consideration of the light and radial velocity curves. The first such object discovered to confirm the theory was KOI 54 (HD 187091, Welsh et al. 2011). Subsequently, more tidally interacting eccentric binary systems have been discovered in the *Kepler* field as well as in the Magellanic clouds from OGLE observations by Thompson et al. (2012), Hambleton et al. (2013) and Nicholls & Wood (2012), respectively. Only observations from *Kepler* provide the temporal resolution to allow for a dedicated seismic analysis for these stars. Table 1 lists several newly-found heartbeat stars in the *Kepler* field of view with a component exhibiting solar-like oscillations.

The seismic study of a sample of 18 eccentric systems (Fig. 2) is presented in Sect. 3. For a detailed seismic study,
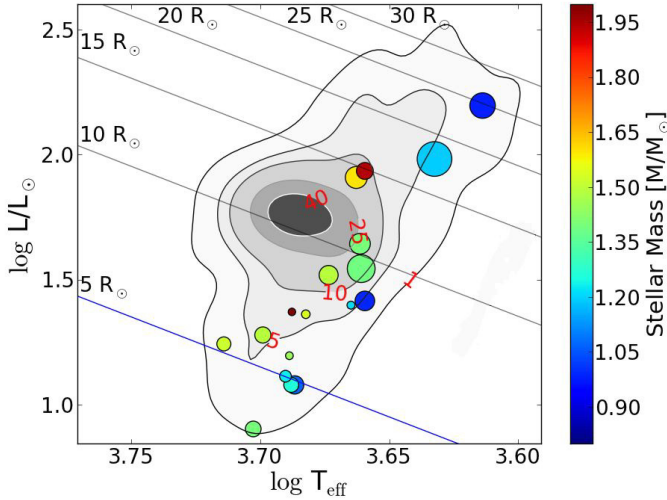
Fig. 2. Position of the 18 red giant heartbeat stars from Tables 1 and 2 in the HR diagram, where the colour shows the mass of the red giant, derived from seismology. The size of the dots represents the orbital period, ranging between 20 and 438 d. The contour surfaces reflect the density distribution of 1000 pulsating red giants. The darkest areas mark the position of the densely populated red clump. Numbers in red indicate the star count per bin, for which the contour surfaces have been drawn. Lines of equal radii in the HR diagram have been drawn for selected stellar radii between 5 and 30 $R_\odot$.

a large number of oscillation modes is needed to allow for an optimal comparison with theoretical models. The star with the richest power density spectrum is KIC 5006817. Sections 4–6 describe the seismic, spectroscopic and binary analyses of this system. The results of these different analyses are compared in Sect. 7. In Sect. 8 we reflect upon the possibility that heartbeat stars are potential subdwarf B (sdB) and cataclysmic variables (CV) progenitors.

2. Observations

The *Kepler* datasets used in this study cover a time base up to 1300 d (Quarters Q0–Q14) in the long cadence observing mode of *Kepler*. In this mode, integrations of 6.04 s are taken every 6.54 s and 270 such integrations are co-added for transmission to Earth to give an integration time of 29.43 min, leading a Nyquist frequency of 283.4 μHz. For one target a month of short cadence data was available. In this observing mode, the individual integrations are stacked to exposures of 58.8 s, which leads to a Nyquist frequency of 8495 μHz (Fig. 3). To produce light curves which are robust against long period instrumental drifts, we extracted the photometric flux from the pixel data following the methods described by Bloemen (2013). The light curves were corrected following García et al. (2011). The target pixel data were also used to inspect whether the light curve was contaminated by neighbouring field stars. In all cases a significant contamination is unlikely.

Red giant heartbeat candidates were selected by inspecting the light curves. Also the subsequent versions of the *Kepler* eclipsing binary catalogue (Prša et al. 2011; Slawson et al. 2011; Matijevič et al. 2012) were searched for candidates among the stars classified as red giants.

The light curves of red giant stars are dominated by the low frequency signals of the granulation background and of the solar-like oscillations (Fig. 4), which hamper a determination of the precise value of the orbital period from the reoccurring
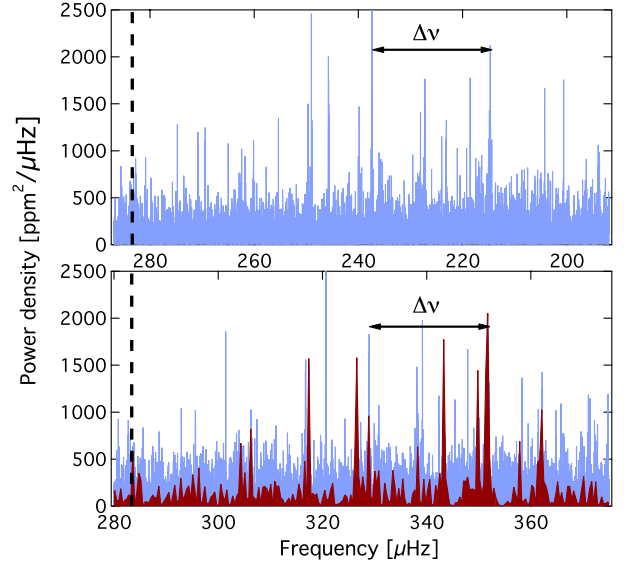

Fig. 3. Power density spectra of KIC 8803882 from 1250 d of long and 30 d of short cadence data are shown in blue and red, respectively. The formal Nyquist frequency (dashed line) separates the reflected oscillation power (*top panel*, sub-Nyquist frequency range) and the original power excess (*bottom panel*, super-Nyquist frequency range).
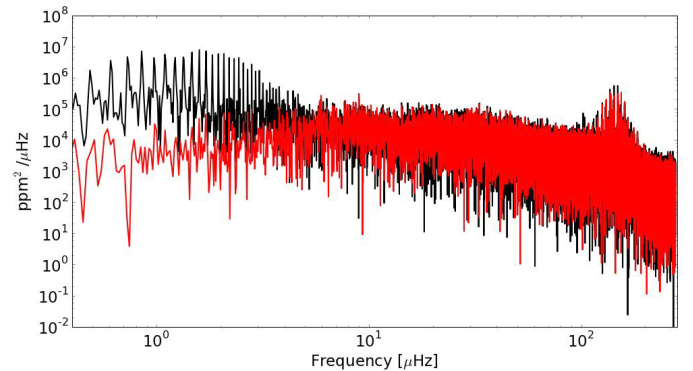

Fig. 4. Power density spectrum (PDS) of the light curve of KIC 5006817. The black PDS was calculated from the original light curve. The red PDS originates from a high-passband filtered light curve, corrected for the mean flux variation during the periastron passage. A zoom into the power excess is shown in Fig. 5.

flux modulation at periastron (hereafter referred to as *heartbeat event*). Therefore, the light curves were smoothed with a boxcar with a width of a few days and analyzed using the phase dispersion minimisation technique (Stellingwerf 1978). By testing for strictly periodic recurrences, confusion with other variability sources, such as stellar activity or instrumental artefacts is excluded.

For an independent confirmation of the binary nature of the discovered heartbeat systems, we searched for radial velocity variations from spectra obtained with the Hermes spectrograph (Raskin et al. 2011), mounted on the 1.2 m *Mercator* Telescope at La Palma, Canary Islands, Spain. This highly efficient échelle spectrograph has a resolving power of $R = 86\,000$. The raw spectra were reduced with the instrument-specific pipeline. The radial velocities were derived through weighted cross-correlation of the wavelength range between 478 and 653 nm of each spectrum with an Arcturus template (Raskin et al. 2011). For our prime target, KIC 5006817, two orbital cycles were monitored

Table 1. Seismic and fundamental parameters for 14 oscillating red giant heartbeat stars, ordered by descending orbital period.

Star KIC	ν_{max} [μHz]	$\Delta\nu$ [μHz]	$\Delta\Pi_1$ [sec]	δf_{max} [nHz]	Evol. phase	R [$R_\odot$]	M [$M_\odot$]	$\log g$ [dex]	L [$L_\odot$]	T_{eff} [K]	P_{orbit} [d]	A [ppt]	$|\Delta RV|$ [km s^{-1}]
9151763	13.8 ± 0.2	1.98 ± 0.01	–	–	RGB?	17.6 ± 0.4	1.19 ± 0.08	2.01	96 ± 16	4290	437.5	+7.1	32.2
7431665	54.0 ± 0.7	5.46 ± 0.02	~67	–	RGB	9.4 ± 0.1	1.39 ± 0.05	2.62	35 ± 2	4580	281.4	–3.0	[37.8]
5039392	6.2 ± 0.1	1.13 ± 0.01	–	–	RGB	24.0 ± 0.7	0.98 ± 0.07	1.67	157 ± 24	4110	236.7	–6.0	42.3
9540226*	27.4 ± 0.4	3.18 ± 0.01	–	–	RGB	14.1 ± 0.3	1.6 ± 0.1	2.37	81 ± 13	4600	175.4	–7	45.3
8210370	44.1 ± 0.8	4.69 ± 0.02	–	–	RGB?	10.5 ± 0.2	1.40 ± 0.08	2.54	44 ± 4	4585	153.5	–5.3	22.1
11044668	50.2 ± 0.2	5.65 ± 0.01	~60	83(?)	RGB	8.18 ± 0.09	0.99 ± 0.03	2.59	26 ± 3	4565	139.5	–3.8	[43.0]
10614012*	70.2 ± 0.9	6.54 ± 0.02	–	–	RGB	8.6 ± 0.2	1.49 ± 0.08	2.74	33 ± 4	4715	132.1	–4.7	49.3
9163796	153.2 ± 0.7	13.53 ± 0.04	–	–	RGB	4.46 ± 0.03	0.89 ± 0.01	3.09	12 ± 1	4820	121.3	± 0.5	70.1
2444348	30.5 ± 0.3	3.26 ± 0.01	–	–	RGB	14.9 ± 0.3	1.94 ± 0.11	2.38	86 ± 14	4565	103.5	–1.7	7.7
5006817	145.9 ± 0.5	11.64 ± 0.01	78	450	RGB	5.84 ± 0.09	1.49 ± 0.06	3.08	19 ± 3	5000	94.8	–1.7	23.5
8803882	347 ± 3	22.6 ± 0.4	–	500(?)	RGB	3.68 ± 0.1	1.4 ± 0.1	3.45	8 ± 1	5043	89.7	+0.5	[1.9]
8144355	179 ± 2	13.95 ± 0.04	~78	210(?)	RGB	4.90 ± 0.09	1.26 ± 0.08	3.16	12 ± 2	4875	80.6	+2.1	18.9
9408183	164.8 ± 0.2	13.29 ± 0.02	~93	450	RGB	5.02 ± 0.07	1.23 ± 0.05	3.12	13 ± 1	4900	49.7	+1.5	64.4
2720096	110.1 ± 0.7	9.17 ± 0.01	–	–	RGB	6.98 ± 0.08	1.54 ± 0.06	2.95	23 ± 2	4812	26.7	+1.0	4.0
8095275	69.3 ± 0.3	6.81 ± 0.01	–	–	RGB	7.78 ± 0.08	1.21 ± 0.05	2.74	25 ± 3	4622	23.0	–6.0	20.6

Notes. The star's identifier in the *Kepler* Input Catalogue (KIC) is given. Eclipsing systems are marked with an asterisk. The columns ν_{max} and $\Delta\nu$ report the frequency of the oscillation power excess and the large frequency separation between radial modes for a given star. $\Delta\Pi_1$ quantifies the true period spacing of dipole modes. The maximum value of the detected rotational splitting δf is listed. The evolutionary phase RGB describes H-shell burning red giant. Ambiguous values are marked with "?". The columns R, M, L, and $\log g$ report the stellar radius, mass, luminosity, effective temperature and surface gravity from scaling relations, respectively. T_{eff} was adopted from the KIC. The uncertainties of $\log g$ are on the order of 0.01 dex and for the temperature typically smaller than 150 K. P_{orbit} gives the orbital period from photometry. The column A lists the maximum amplitude of the heartbeat in a rebinned phase diagram. The error estimate for P_{orbit} and A from the PDM is not reliable due to the remaining contamination of the solar-like oscillations and therefore not given. $|\Delta RV|$ reports the maximum difference in radial velocity. Square brackets mark systems for which the orbital parameters could not yet be determined from radial velocities.

Table 2. Low-luminosity red giants with ν_{max} higher than 283 μHz from long cadence data.

Star KIC	f_{max} [μHz]	(ν_{max}) [μHz]	$\Delta\nu$ [μHz]	R [$R_\odot$]	M [$M_\odot$]	$\log g$ [dex]	L [$L_\odot$]	T_{eff} [K]	P_{orbit} [d]	A [ppt]	$|\Delta RV|$ [km s^{-1}]
7799540	220 ± 5	(347.2)	24.0	3.64	1.52	3.50	17.5	5177	71.8	+0.5	[31.8]
2697935*	161 ± 3	(405.6)	~28	3.26	1.45	3.574	15.7	4883	21.5	±1.3	52.1
8912308	217 ± 9	(350.2)	22.7	4.20	2.02	3.50	23.5	4872	20.2	+1.2	61.4

Notes. The definition of columns KIC, $\Delta\nu$, M, R, $\log g$, L, P_{orbit}, A and $\Delta|RV|$ is the same as in Table 1. f_{max} and (ν_{max}) indicate the frequency of the maximum oscillation power, reflected at the Nyquist frequency and reconstructed power excess, respectively. T_{eff} was adopted from the KIC parameters. The uncertainties of M, R, $\log g$ and L are better than 2, 5, 1, and 15 per cent, respectively.

Table 3. Orbital parameters for systems for which the periastron has been monitored with the Hermes spectrograph.

Star KIC	n_{RV}	P_{orbit} [d]	e	Ω [rad]	K [km s^{-1}]	γ [km s^{-1}]	T_0 [HJD]	Eclipse duration
9151763	24	437.51 ± 0.03	0.73 ± 0.01	3.03 ± 0.01	16.20 ± 0.04	–92.89 ± 0.03	2 455 949.64 ± 0.06	
5039392	13	236.70 ± 0.02	0.44 ± 0.01	4.96 ± 0.01	22.6 ± 0.2	–14.96 ± 0.05	2 454 874.2 ± 0.27	
9540226*	31	175.43 ± 0.01	0.39 ± 0.01	0.07 ± 0.01	23.32 ± 0.04	–12.37 ± 0.02	2 456 425.89 ± 0.09	P: 4 d; S: 3 d
8210370	16	153.50 ± 0.01	0.70 ± 0.01	1.17 ± 0.01	12.96 ± 0.36	–0.76 ± 0.08	2 454 937.35 ± 0.01	
10614012*	22	132.13 ± 0.01	0.71 ± 0.01	1.23 ± 0.01	24.68 ± 0.03	–0.92 ± 0.02	2 454 990.48 ± 0.01	1 d
9163796	17	121.30 ± 0.01	0.69 ± 0.01	0.00 ± 0.01	35.64 ± 0.01	–11.05 ± 0.01	2 456 409.60 ± 0.01	
2444348	17	103.50 ± 0.01	0.48 ± 0.01	4.30 ± 0.01	4.76 ± 0.02	14.47 ± 0.01	2 454 947.74 ± 0.09	
5006817	70	94.812 ± 0.002	0.7069 ± 0.0002	4.0220 ± 0.0005	11.709 ± 0.005	–14.021 ± 0.002	2 456 155.924 ± 0.002	
8144355	19	80.55 ± 0.01	0.76 ± 0.01	2.79 ± 0.01	9.44 ± 0.04	0.02 ± 0.03	2 455 914.43 ± 0.02	
9408183	7	49.70 ± 0.01	0.42 ± 0.01	0.17 ± 0.01	37.17 ± 0.04	–14.37 ± 0.01	2 454 989.80 ± 0.01	
2720096	13	26.70 ± 0.01	0.49 ± 0.01	6.11 ± 0.01	2.28 ± 0.03	9.92 ± 0.01	2 454 990.67 ± 0.05	
8095275	25	23.00 ± 0.01	0.32 ± 0.01	2.19 ± 0.01	10.50 ± 0.06	–8.58 ± 0.03	2 454 971.02 ± 0.03	
2697935*	27	21.50 ± 0.01	0.41 ± 0.02	2.33 ± 0.06	26.5 ± 0.6	–74.4 ± 0.4	2 454 990.9 ± 0.1	0.1 d
8912308	28	20.17 ± 0.01	0.23 ± 0.01	3.34 ± 0.01	30.78 ± 0.02	–52.69 ± 0.01	2 454 994.06 ± 0.01	

Notes. Number of radial velocity measurements, n_{RV}; orbital period P_{orbit}; eccentricity e; argument of periastron Ω; radial velocity amplitude K; velocity of the system γ; and zero point T_0. The duration of the eclipse is given. P and S indicate the primary and secondary eclipses, respectively.

Table 4. Inclination values for individual pressure-dominated modes.

$m = 0$	Inclination
137.02	70.2 ± 5
137.93	76.3 ± 5
148.29	82.9 ± 4
149.19	80.2 ± 4
mean	77 ± 9

Notes. Individual inclinations for the pressure-dominated dipole modes, centred on the $m = 0$ component, in the range between 130 and 155 μHz (Fig. 7).

Table 5. Fundamental parameters of the red giant KIC 5006817.

T_{eff} [K]	$\log g$[dex]	[Fe/H] [dex]	v_{micro} [km s^{-1}]	LB [km s^{-1}]
5000 ± 250	3.0 ± 0.5	-0.06 ± 0.12	3.0 ± 0.5	8 ± 1

Notes. Results for the effective temperature T_{eff}, surface gravity $\log g$, and microturbulence v_{micro} of the red giant component. The last column gives the total line broadening as defined in Sect. 5.1.

in 2012 as well as in 2013. Radial velocity monitoring for the other stars listed in Table 1 is ongoing. Tables 1 to 3 report the first orbital results for stars in our sample.

3. Eccentric red giant systems in the *Kepler* data

In total, we found 18 red giant stars in eccentric binary systems that show the characteristic gravitational distortion of heartbeat stars. These stars were found in a sample of *Kepler* red giants that encompass about 16 000 stars. All stars show the clear signature of solar-like oscillations (Tables 1 and 2). Figure 1 shows phase diagrams of five selected stars.

The global seismic analysis of red giant stars enables us to accurately constrain the fundamental parameters of the main component of the binary system. The characteristic comb-like structure of solar-like oscillations originates from p modes and therefore depends on the sound speed in the acoustic cavity. The main characteristics of the power excess (central frequency of the oscillation power excess, ν_{max}, and the large frequency separation between consecutive radial modes, $\Delta\nu$) scale well with the mass and radius, and to a lesser extent with effective temperature (e.g. Kjeldsen & Bedding 1995; Mosser et al. 2013). Following the approach of Kallinger et al. (2010b) we estimated the radius, mass, luminosity, $\log g$ and effective temperature of our sample stars (Tables 1 and 2) and place the red giant components of the binaries in the Hertzsprung-Russell (HR) diagram shown in Fig. 2. All stars except two have masses between 1 and 1.5 $M_\odot$. The majority of the *Kepler* red giants are located in this mass range.

3.1. Evolutionary status of red giant heartbeat stars

Seismic information can reveal the evolutionary status of the star. Stars with a large frequency separation $\Delta\nu \gtrsim 9\,\mu$Hz (i.e. $R_{\mathrm{RG}} \lesssim 7\,R_\odot$) are located well below the red clump (Fig. 2) and therefore can only be in the hydrogen shell burning phase. A value of $\Delta\nu \lesssim 3\,\mu$Hz (i.e. $R_{\mathrm{RG}} \gtrsim 13\,R_\odot$) occurs for stars located above the red clump. Such stars are likely to be H-shell burning stars, high up on the RGB, although in principle they also could be stars on the low asymptotic giant branch (AGB). Stars with frequency separation $3 \lesssim \Delta\nu \lesssim 9\,\mu$Hz can also be in the helium core burning phase (Bedding et al. 2011; Mosser et al. 2012b).

Therefore, a further criterion to determine the evolutionary state of stars with radii larger than $7\,R_\odot$ is needed.

The period separation of mixed dipole modes is a powerful diagnostic to distinguish between hydrogen shell and helium core burning stars (cf. Bedding et al. 2011; Mosser et al. 2011b). The true period spacing $\Delta\Pi_1$ describes the constant period spacing of pure dipole g modes, which cannot be observed directly. However, one can determine the value of $\Delta\Pi_1$ by fitting a theoretical mixed mode pattern to the actually observed modes in the power spectrum (Mosser et al. 2012a). Stars which exhibit a value of $\Delta\Pi_1 \lesssim 100$ s are burning hydrogen in a shell around the inert helium core, while stars with a larger $\Delta\Pi_1$ value belong to stars on the AGB or RC. The estimated values of the true period spacing $\Delta\Pi_1$ for the pulsators are given in Table 1.

Several stars do not or barely show dipole mixed modes and it is impossible to recover their mixed mode pattern. For these stars we did not determine the evolutionary state from the period spacing but used the phase shift (ϵ_c) of the central radial mode as an indicator. Kallinger et al. (2012) have shown that in a diagram of ϵ_c versus the large separation $\Delta\nu$, the stars fall into groups which can be identified as H-shell burning, He-core burning and AGB stars. For most stars, the identification of the evolutionary stage from ϵ_c and the observed period spacing are in agreement. Therefore we are also able to estimate the evolutionary state of stars which did not show a clear forest of dipole modes.

For nearly all heartbeat red giants we could constrain them to be in the state of H-shell burning. The remaining stars are also likely to be in the same evolutionary state but we cannot rule out more evolved phases. Among our sample there are 5 stars in a $\Delta\nu$ range where the stars can either be an RGB or RC star. Statistically there is a chance of about 70 per cent that a given red giant in this range burns He in its core (Kallinger et al. 2012). Even though the number statistics are still poor we find clear preference for RGB primaries in heartbeat stars. In Sect. 8, we discuss that this could be a result of binary evolution.

3.2. Giants with power excess above the formal Nyquist frequency

In the power density spectrum of KIC 8803882, we find a reverse combination of $l = 2$ and 0 modes with respect to the known comb-like structure between 200 μHz and the LC-Nyquist frequency of 283 μHz with an apparent large separation of $\Delta\nu = 22.7\,\mu$Hz (Fig. 3). Stars which show similar structures in their power spectra are KIC 8912308, KIC 2697935 and KIC 7799540 (cf. Table 2).

As the dataset of KIC 8803882 contained a month of short cadence observations (Q14.1), we could compare the analysis of the super Nyquist frequency range from long cadence data with the same, well resolved frequency range from short cadence data. This comparison, depicted in Fig. 3, allows us to explore the frequency range above the formal Nyquist frequency, $\nu_{\mathrm{Nyquist}} = 283\,\mu$Hz for long cadence data (Murphy et al. 2013). We determined the large separation $\Delta\nu$ through manual peakbagging of the long cadence data to be 22.7 μHz, which is in perfect agreement with the large separation of 22.65 μHz from short cadence data. The standard approach to determine the frequency of the power excess (e.g. Kallinger et al. 2010b) uses a simultaneous fit of the Gaussian envelope, multiple power laws for the background and a white noise component. In the super Nyquist frequency domain, we find an artificial background with increasing power density towards higher frequencies as the signal of the low frequency domain is mirrored. Therefore, we determined the position of ν_{max} by fitting a broad Gaussian to the reflected signal

and calculated the true frequency of the power excess,

$$\nu_{max}^{true} = 2 \cdot \nu_{Nyquist} - \nu_{max}^{reflected}. \tag{1}$$

From the values obtained for KIC 8803882, KIC 8912308, KIC 2697935, and KIC 7799540 (cf. Tables 1 and 2) we conclude that they are low-luminosity red giants.

4. Case study of KIC 5006817

While ensemble asteroseismology allows the easy characterisation of large samples of red giant stars (e.g. Huber et al. 2011; Hekker et al. 2011; Kallinger et al. 2010b; Mosser et al. 2012a), studies of individual stars in a close binary grant us additional insight into the structure of the primary as well as the interaction between the binary system components. As a proof-of-concept of what such objects have to offer compared to single pulsators, we organised a spectroscopic campaign on the heartbeat star with the richest oscillation pattern, KIC 5006817.

The power density spectrum of the *Kepler* observations of KIC 5006817 is shown in Fig. 4. It contains power excess centred around $146\,\mu$Hz. Apart from the typical granulation signal and a series of low frequency peaks ($<10\,\mu$Hz) originating from the heartbeat event, no other significant frequencies are present (Fig. 4). The oscillation power excess itself is typical for a red giant primary. The frequency range of the excited oscillation modes is shown in Fig. 5. For a detailed asteroseismic analysis, only modes with a signal of at least 8 times the background level were extracted. The frequencies of the individual modes were extracted as the centroid of the power density in narrow predefined windows, which we checked for consistency by fitting Lorentzian profiles to a number of modes.

KIC 5006817's seismic mass and radius estimates are $1.49 \pm 0.06\,M_\odot$ and $5.84 \pm 0.09\,R_\odot$, respectively (Table 1). The true period spacing of 78 s indicates that the star is in the phase of H-shell burning (Bedding et al. 2011; Mosser et al. 2012b). In the HR Diagram shown in Fig. 2, this star is located well below the red clump.

4.1. Seismic information on the stellar rotation

The power density spectra of many red giants contain clear signatures of the rotational splitting of nonradial modes, which enables us to learn more about the internal rotation of those stars. This effect arises as rotation breaks the degeneracy of nonradial modes by shifting the mode frequencies of the components with azimuthal order $m \neq 0$ away from the central multiplet frequency $(m = 0)$:

$$f_{n,\ell,m} = f_{n,\ell,0} + \delta f_{n,\ell,m}, \tag{2}$$

with the rotational splitting $\delta f_{n,\ell,m}$ given by

$$\delta f_{n,\ell,m} = m \cdot \frac{\Omega}{2\pi} \cdot (1 - C_{nl}), \tag{3}$$

where Ω is the average rotation frequency in the cavity in which a given mode propagates and C_{nl} is the Ledoux constant (Ledoux 1951). The values of the rotational splittings reported in this work are taken to be equal to the frequency separation between two consecutive multiplet components (i.e. $|\Delta m| = 1$). If no central peak ($m = 0$) is detected, we take half the value of the frequency difference between outer dipole components. We refer to such values as the normalised rotational splitting. In the power density spectrum of KIC 5006817, we find rotationally
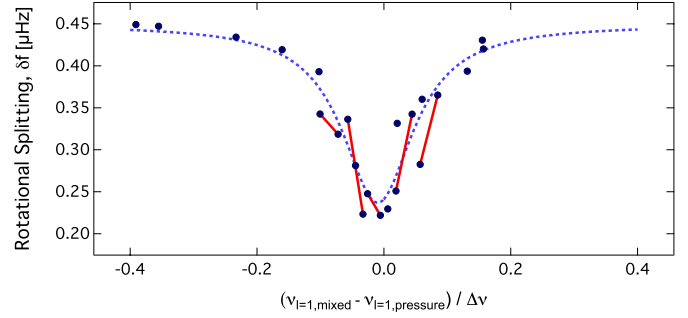
Fig. 6. Splitting-échelle diagram of rotationally affected dipole modes in KIC 5006817. Measured rotational splittings are shown as dots. Solid lines connect two splittings originating from the same dipole mode triplet. The *x*-axis gives the position of a rotationally split dipole mode $\nu_{l=1,mixed}$ with respect to the pure pressure dipole mode $\nu_{l=1,pressure}$ and as fraction of the large frequency separation $\Delta\nu$. The dashed line describes the modulation of the rotational splitting through a Lorentz-profile (Mosser et al. 2012a).

split modes of the spherical degree $\ell = 1$. The multiplet structure in $l = 2$ can originate from splitting or mixed modes. In principle, also $\ell = 3$ modes should be split. However, we have no clear identification of them as in this star $l = 3$ modes have amplitudes close to the significance limit.

As g-dominated and p-dominated modes are sensitive to the rotation in the central and outer regions of the star, respectively, they can be used to probe the internal rotation gradient. Beck et al. (2012) showed that larger splitting of g-dominated than of p-dominated dipole modes, as found in KIC 5006817 (Figs. 6 and 7) reveals that its interior, rotates multiple times faster than its envelope.

For some dipole multiplets the presence of a significant central peak ($m = 0$) allowed us to measure the individual splittings for the $m = -1$ and $+1$ components, revealing asymmetries. Such pairs of splittings are connected with a solid line in Fig. 6. As rotation shifts the frequency of modes, each mode within a triplet has a slightly different oscillation cavity, which also modifies its mixed character in terms of p- and g-mode components. The asymmetries are mirrored around the pure p mode and follow the Lorentzian description (Fig. 6).

The smallest measured rotational splitting of dipole modes is about $0.21\,\mu$Hz and was measured in two asymmetric p-mode dominated mixed modes. This is about 2.25 times smaller than the largest splitting δf_{max} of $0.45\,\mu$Hz found for g-mode dominated dipole modes. The largest splitting values (δf_{max}) originating from the g-mode dominated dipole modes are consistent with those measured for large samples of single pulsating red giants (e.g. Beck et al. 2012; Mosser et al. 2012a)

The extracted rotational splitting of dipole modes (Fig. 6), shows the expected modulation as a function of the degree of mixed character (Mosser et al. 2012b,a). The mode identification from the universal red giant oscillation pattern for pressure modes (Mosser et al. 2012a), and from asymptotic expansion for mixed modes and the rotational splittings (Mosser et al. 2012a,b) is indicated with vertical bars in Fig. 5. We note that a perfect fit is not needed to identify the modes.

4.2. Testing of the rotational profile from forward modelling

Because of the conservation of angular momentum, one expects the core of a red giant to rotate significantly faster than its surface. Previous analyses (Beck et al. 2012; Deheuvels et al. 2012; Mosser et al. 2012a) only revealed the ratio of the
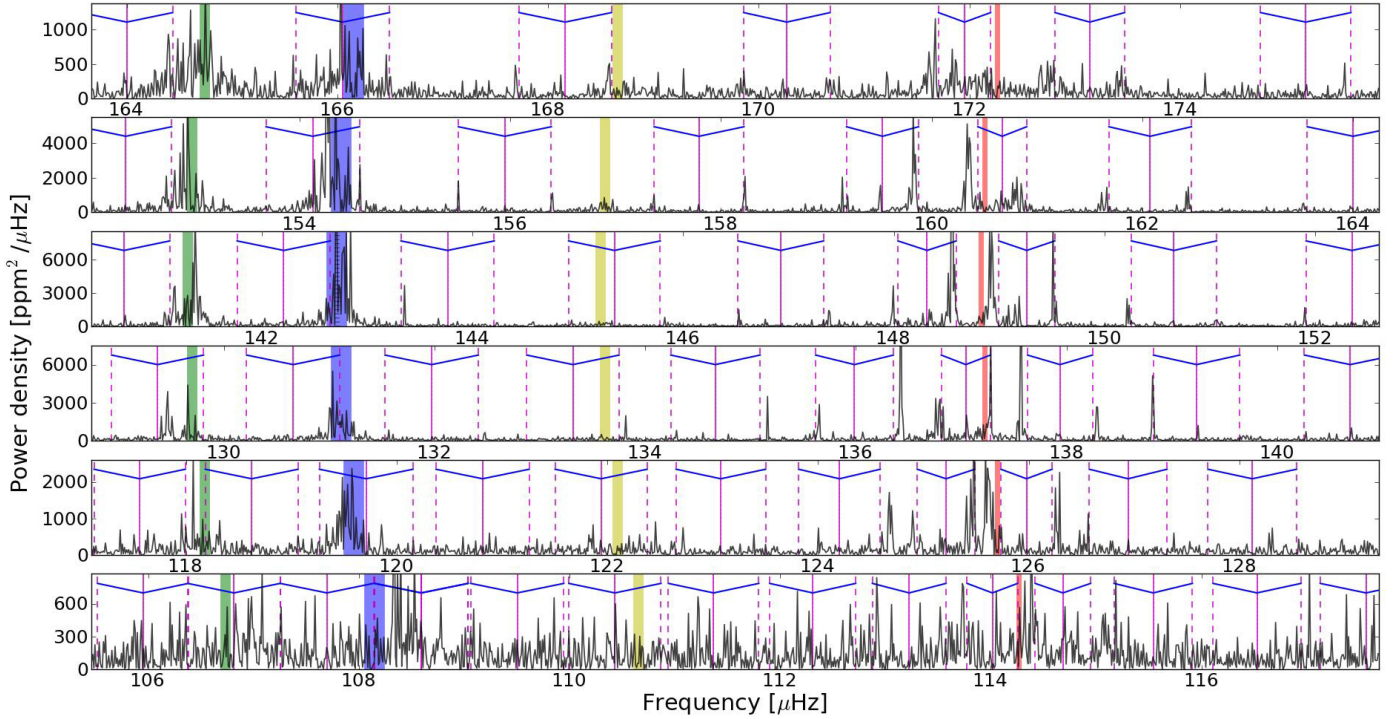
Fig. 5. Power density spectrum (PDS) of KIC 5006817 (Q0–Q13). Each panel contains one radial order. Mode identifications of the pure p modes come from the universal frequency pattern (Mosser et al. 2011b) for $\ell = 0$, 1, 2 and 3 and are indicated with blue, red, green and yellow vertical bars, respectively. The effects of rotation are visible as the splitting of dipole modes, located in the centre of each panel. The observed PDS is overlaid with the theoretical frequencies of mixed dipole modes ($m = 0$, solid thin lines) and the theoretical frequencies of the rotationally split components ($m = \pm 1$, dashed thin lines) which have been calculated using methods described by Mosser et al. (2012a,b). The components belonging to one rotationally split multiplet are indicated through V-markers at the top of each panel.

core-to-surface rotation rate, rather than the shape of the rotational gradient in the transition region between the faster rotating core and the slower rotating envelope. Goupil et al. (2013) propose a way to infer directly the ratio of the average envelope to core rotation rates from the observations. In this paper, we take a different approach by using forward modelling.

In principle, the number of rotationally split modes in KIC 5006817 and their different degree of mixed character (and therefore different "sensitivity" to internal layers of the star) should enable us to probe the rotation rate at different depths of the star, i.e. to resolve the rotational gradient to more than a ratio between the core and surface value. The radial structure of a red giant is dominated by a helium core and an extended convective envelope. To mimic this structure we considered models consisting of consecutive shells, which are each assumed to rotate rigidly, but with different angular velocities.

We computed such a representative $1.5\,M_\odot$ model using the Yale Stellar Evolution Code (YREC; Demarque et al. 2008; Guenther et al. 1992). The model was selected to approximately reproduce the observed radial modes and true dipole period spacing of KIC 5006817, where we note that no "exact" match is necessary as the mode eigenfunctions (and therefore the rotational kernels) of similar models are almost identical (see also Deheuvels et al. 2012). Our representative model was computed for near solar composition ($Z = 0.02$, $Y = 0.28$) assuming the solar mixture by Grevesse et al. (1996) and a mixing length parameter ($\alpha_{\mathrm{MLT}} = 1.8$). The model has a radius, effective temperature, age, and inert He core mass fraction of about $5.8\,R_\odot$, 4855 K, 2.8 Gyr, and 0.14, respectively. More details about the input physics of the model are given in Kallinger et al. (2010a).

We focussed on the two radial orders (i.e. the frequency range of $\sim$130 to $\sim$155 μHz), in which 9 rotationally split dipole

modes with good signal-to-noise were extracted. Additionally, we tested if rotational splittings from two $\ell = 2$ modes can be measured. In Fig. 7 we show the power density spectrum of the two radial orders of KIC 5006817 along with the mode inertia of the $\ell = 0$ to 3 modes computed for our representative model, in the adiabatic approximation.

In order to determine which layers dominate the rotational splitting of a given mode, we computed the adiabatic eigenfunctions for the 9 dipole and 2 quadrupole modes (using the nonradial nonadiabatic stellar pulsation code by Guenther 1994) as well as their rotational kernels. The integrated and normalised kernels are shown as a function of the fractional radius in Fig. 8, illustrating that all dipole modes contain a significant contribution from the fast rotating core region, even the most p-mode dominated ones (indicated as d3 and d7). The kernels are almost flat in the radiative region of the envelope (between the two dashed vertical lines). This is in agreement with the analysis of the kernels for KIC 8366239 (Beck et al. 2012). The dipole splittings provide an upper limit for the surface rotation rate. More promising are the $\ell = 2$ kernels, but even those contain significant contributions from the core and from the inner part of the convective envelope.

For a better quantitative result, we deduce the rotation profile $\Omega(r)$ such that

$$\delta f_{n,\ell} = \frac{1}{2\pi I_{n,\ell}} \int_{r=0}^{R} K_{n,\ell}(r)\Omega(r)\mathrm{d}r, \qquad (4)$$

is satisfied for the measured splittings. Here $I_{n,\ell}$ and $K_{n,\ell}$ are the mode inertia and the rotational kernel of a given mode, respectively, and R is the radius of the model. To solve this equation, several inversion techniques have been developed in the past
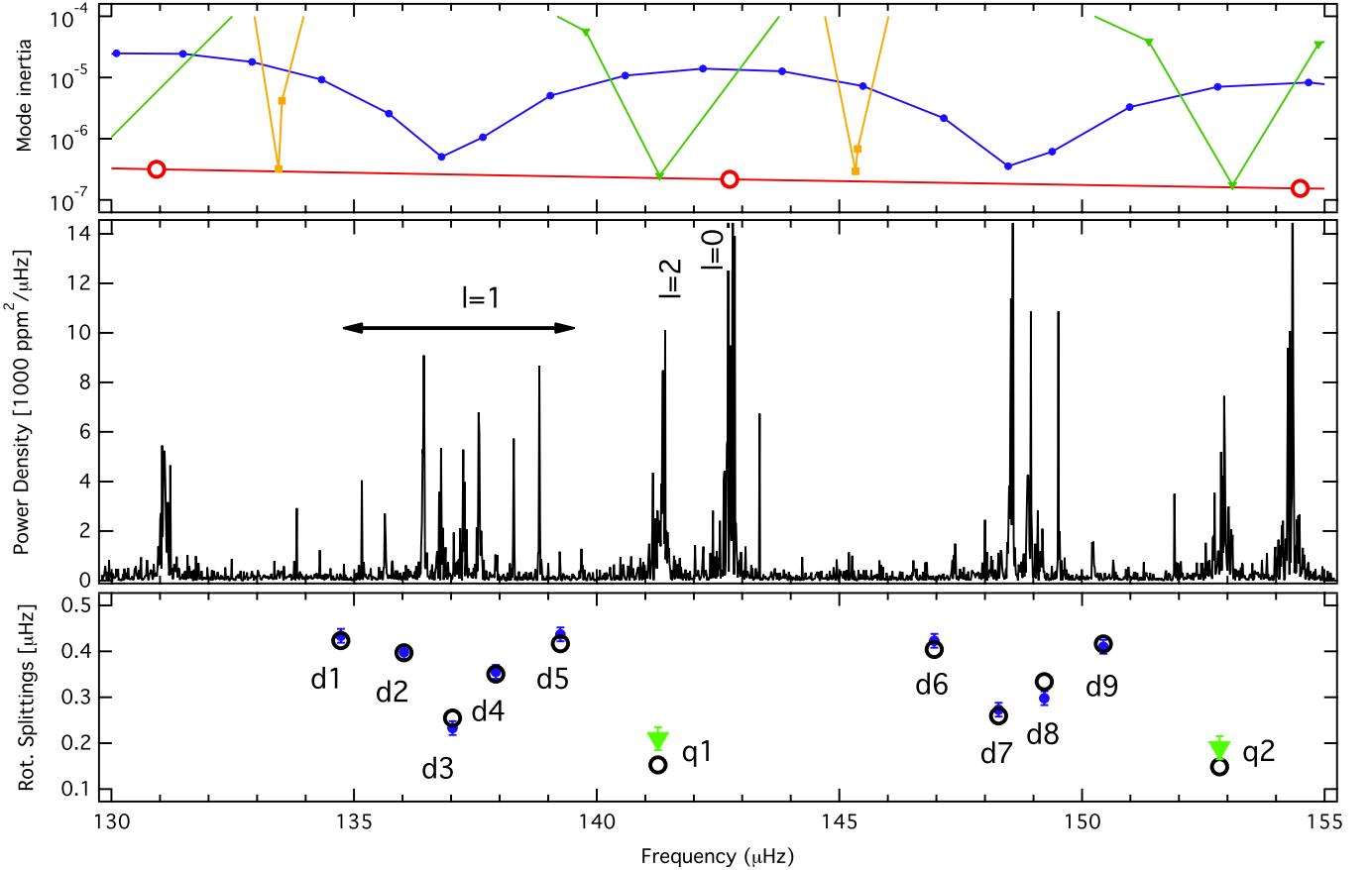
Fig. 7. Frequencies for the two central radial orders of KIC 5006817. *Top panel*: the coloured dots connected with line segments indicate the inertia (right axis with arbitrary scale) of the $m = 0$ adiabatic modes computed for a representative model for KIC 5006817 (red circles, blue filled dots, green triangles, and yellow squares correspond to $\ell = 0, 1, 2$ and 3 modes, respectively). *The middle panel* provides a zoom on the frequencies in the range of the two central radial orders. *Bottom panel*: measured rotational splittings for $\ell = 1$ (blue dots) and 2 (green triangles) modes. Open black circles indicate the splittings that result from our best-fit 2-zone model. Dipole modes are labelled with d, quadrupole modes with q.

with the aim to determine the internal rotation profile of the Sun. A summary how to apply them to an evolved star is available in Deheuvels et al. (2012).

The inversion of the integral in Eq. (4) is a highly ill-conditioned problem and either requires numerical regularisation or localised averages of the true rotation profile in different regions of the star. We used both, adopting the regularised least squares method (RLS; e.g. Christensen-Dalsgaard et al. 1990) and the subtractive optimally localised averages technique (SOLA; e.g. Schou et al. 1998). In doing so, we can determine the core to surface rotation rate. However, as soon as we increased the number of shells, aiming to locate where the transition between fast rotating core and the slowly rotating envelope is taking place, both methods failed. Either the results became numerically unstable or it was impossible to evaluate the reliability of the result.

We therefore chose to apply a Bayesian forward modelling approach. We computed synthetic rotational splittings for a model (using Eq. (4)), which was first divided into several solidly rotating shells, where the rotation rate of each shell was treated as a free parameter. To fit the synthetic splittings to the measured ones, we used a Bayesian nested sampling algorithm called MULTINEST (Feroz et al. 2009) that provides a probability density distribution (PDD) for each fitted parameter, from which we assessed the best-fit values and their uncertainties. The PDDs allowed us to test the reliability of a specific model, e.g. a flat PDD for a specific shell implies that the measured rotational

splittings do not contain information about the rotation rate in this specific region of the star. Additionally, MULTINEST provides the model evidence, which allows us to compare different assumptions for the rotation rates in the shells and evaluate which one reproduces the observations best. We tested different numbers and combinations of shells and found that a 2-zone model (core and envelope) is better by several orders of magnitude. Even introducing regularisation priors (e.g. a smooth gradient between consecutive shells) did not improve the description of $\Omega(r)$.

4.3. Core and surface rotation

The final model we adopted is a 2-zone one with a core (inner 1 per cent in radius or 14 per cent in mass) and an envelope zone, where we found that the placement of the exact position of the border between the two zones only marginally influences the result. Our best fit constrained the rotation frequency (or period) for the core and the envelope to be $0.93 \pm 0.02 \, \mu$Hz (~12.5 d) and $0.07 \pm 0.02 \, \mu$Hz (~165 d), respectively. This corresponds to a core-to-surface rotation rate of about 13. The envelope rotation rate is an average value for 99 per cent of the radius of the star and very likely overestimates the true surface rotation. This asteroseismic result points towards a surface rotation velocity of $1.9 \, \mathrm{km \, s^{-1}}$.

Including the two $\ell = 2$ modes only marginally affects the rotation rate but increases the uncertainty, which is why they
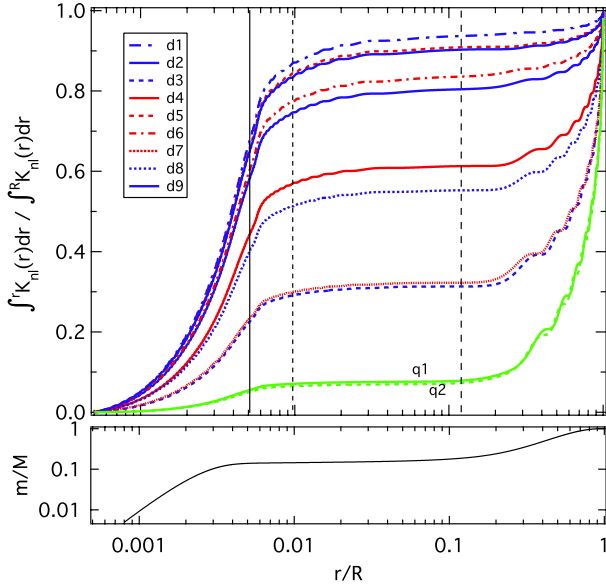
Fig. 8. Normalised integrated rotation kernels of the dipole $\ell = 1$ (blue and red) and quadrupole $\ell = 2$ modes (green) for the two central radial orders as a function of fractional radius. The kernel labels refer to modes in Fig. 7. The vertical lines indicate from left to right the border of the He core (solid line), the H-burning shell (short-dashed line), and the base of the convective envelope (long-dashed line). *Bottom panel*: the model's fractional mass as a function of the fractional radius. The labels (not the colours) of dipole and quadrupole modes are consistent with Fig. 7.

were not taken into account for the final result. We conclude that the currently available observations do not allow us to assess the detailed rotational gradient in the envelope of KIC 5006817, as it was possible for the Sun. We are limited to describing the rotational profile of red giants with a step function.

4.4. Inclination of the axis of rotation and pulsation

The inclination angle of the rotation axis towards the observer can be deduced from the rotational splittings. For solar-like oscillators, the excitation of all $2 \cdot \ell + 1$ components and the equipartition of energy is assumed if the time base of the observations resolves the lifetime effects of a mode.

For dipole modes, the inclination is determined by the height of the $m = 0$ and $m = \pm 1$ modes, provided that all components with the same $|m|$ are excited such that they have the same height in power density (Gizon & Solanki 2003; Ballot et al. 2006). We have also shown that each component of a split multiplet has a slightly different cavity which should result in slightly different heights and lifetimes, an effect absent in the Sun as it has no mixed modes. To compensate for these differences, we do not fit the heights of the $m = \pm 1$ in a given mode individually, but force the heights of the fit to be equal.

Simultaneously fitting all dipole modes in at least one radial order compensates in principle the effects of a changing level of mixed character between p and g modes. This transition is symmetrically mirrored around the pure dipole pressure mode. We tested this approach for the radial orders around 135 and 150 μHz, resulting in inclination values of $i_{\text{rot}} = 73° \pm 3°$ and $i_{\text{rot}} = 80° \pm 3°$ respectively. A global fit of both radial orders lead to $i_{\text{rot}}^{\text{global}} = 76° \pm 4°$, assuming alignment of the rotation and pulsation axis. We compare these values to the mean inclination of $i_{\text{rot}}^{\text{mean}} = 77 \pm 9$, obtained from the individual rotational split

multiplets of the pressure-dominated modes in this frequency range (Table 4). These modes have the highest signal and the shortest lifetimes, and therefore are closest to the assumption of equipartition of mode energy. The uncertainty is an underestimate as it was computed adopting the assumptions mentioned above.

5. Spectroscopy of KIC 5006817

To obtain an independent estimate of the eccentricity of the system, KIC 5006817 has been monitored spectroscopically with the Hermes spectrograph (cf. Sect. 2) in 2012 and 2013. The 60 observations span about 160 d, during which the periastron passages were monitored with several observations a night. The radial velocities derived from these spectra are shown in the top panel of Fig. 9.

5.1. Fundamental parameters

The first 44 individual spectra were shifted by the derived radial velocity value and averaged to produce a high signal-to-noise ratio (S/N) spectrum to determine the stellar atmospheric parameters like effective temperature, T_{eff}, surface gravity log g, microturbulence v_{micro} and the total line broadening from rotation and macroturbulence ($v \sin i + v_{\text{macro}}$).

Given the seismic estimate of rotation and inclination, the total line broadening is dominated by macroturbulence. We used the combination of local thermal equilibrium (LTE) Kurucz-Castelli atmosphere models (Castelli & Kurucz 2004) with the LTE abundance calculation routine MOOG by Sneden (1973). A detailed description of all steps needed to derive the atmospheric parameters can be found in, e.g., De Smedt et al. (2012).

The determination of the atmospheric parameters was based upon Fe I and Fe II lines which are abundantly present in red giants spectra. The Fe lines used were taken from VALD linelists (Kupka et al. 2000). We first calculated in MOOG the theoretical equivalent width (EW) of all available Fe I and Fe II in a wavelength range between 400 and 700 nm for a grid, centred on the seismic parameters found (Table 1). The equivalent widths (EW) of lines were measured via direct integration, the abundance of the line was then computed by an iterative process where theoretically calculated EWs were matched to the observed EW. If the calculated EW deviated from the theoretical EW by a factor of 10, the line was rejected due to possible blends. The stellar parameters are listed in Table 5 and are based on the results from 52 Fe I and 32 Fe II lines.

5.2. Spectral disentangling

In order to look for signatures of a companion in our spectra, we used the spectral disentangling (SPD) method as implemented in the FDBINARY code (Ilijic et al. 2004). Being applied in Fourier space, the method provides a self-consistent and fast solution for the individual spectra of stellar components of a multiple system and a set of orbital parameters simultaneously (Hadrava 1995). The SPD method usually requires a time-series of spectra with good, homogeneous orbital phase coverage and delivers high S/N mean spectra of individual components.

We used the highest S/N spectra to perform the spectral disentangling in a wide wavelength range from 480 to 580 nm. The spectra were split into smaller chunks, typically 5 nm wide, to avoid strong undulations in the continuum of the resulting decomposed spectra from which the Fourier-based SPD
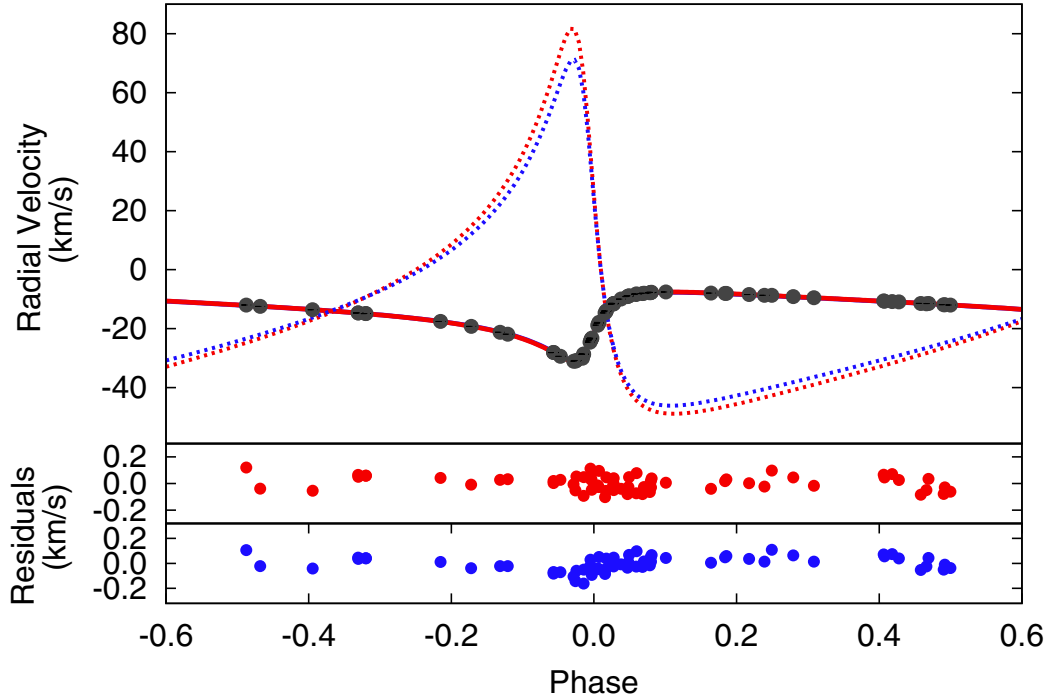
Fig. 9. Radial velocity observations (gray points) with the best-fit model without beaming (solid red line) and with beaming (solid blue line – not visible) phased over 94.82 d. The uncertainty in the radial velocity is smaller than the size of the points. The model with beaming cannot be seen on this scale due to the overlap of the model without beaming. The model of the secondary component is presented for both the beaming (dashed blue line) and non-beaming (dashed red line) best-fit models. *Middle panel*: best-fit residuals of the binary model without beaming (red points). *Lower panel*: residuals of the best-fit binary model with beaming (blue points).

method is known to suffer (see, e.g. Hadrava 1995; Ilijic et al. 2004). Besides the above mentioned metal lines region that also contains the H_β spectral line, we also focussed on a few other regions centred at some helium lines (He I 447, 492, and 502 nm, and He II 469, 541, and 656 nm,) as well as the H_α line. This was done to verify whether the companion could be a white dwarf showing only helium and/or hydrogen lines. In neither of these regions could we detect the lines of the secondary. We estimate the detection limit of the order of 3 per cent of the continuum, which means that any contribution below this level would not be detectable in our rather low S/N spectra ($\simeq 20-30$ in Johnson V).

We also attempted to go beyond our actual detection limit of 3 per cent, by applying the least-squares deconvolution (LSD) method (Donati et al. 1997) to the 44 individual spectra. This method is based on the two fundamental assumptions of self-similarity of all spectral lines and linear addition of blends, and enables the computation of a high-quality average line profile, which is formally characterised by a very high S/N. The first assumption requires hydrogen and helium lines as well as the metal lines with pronounced damping wings to be excluded from the calculations. Moreover, for slowly rotating stars (the case of KIC 5006817), where the rotation is not the dominant source of the line broadening, the selfsimilarity is only applicable to the lines of (nearly) the same strengths. To account for this, we introduced a multiprofile technique as described by Kochukhov et al. (2010), which enables the computation of several average profiles simultaneously for several sets of spectral lines grouped, e.g. according to their relative strengths. The model is then represented as a convolution of the computed mean profiles with the *line mask* which contains information about the position of individual lines as well as their relative strengths.

Furthermore, part of the lines in the spectrum (e.g. those with overlapping absorption coefficients) add up non-linearly which

requires a revision of the second fundamental assumption of the technique. In order to account for the model imperfections due to non-linear blending of the lines, we additionally fitted strengths of the individual lines from the mask to match the observations. This improved procedure (for more details, see Tkachenko et al. 2013) provided us with high S/N (of the order of $450-500$) LSD model spectra which we then used for the SPD in three metal lines regions. Similar to our previous experience with the original spectra, we got a null result, in the sense that no signature of the secondary has been detected, this time, in the high S/N composite spectra. In this case, our detection limit is estimated to be of the order of 1 per cent of the continuum, which is mainly due to the imperfect continuum normalisation rather than the observational noise. We thus conclude that KIC 5006817 is a single-lined spectroscopic binary.

6. Binary parameters of KIC 5006817

The morphology of the photometric light curve is a consequence of ellipsoidal modulation in an eccentric system. The shape of the "heartbeat" feature in the light curve is a function of the inclination, which dictates the peak to dip ratio; the eccentricity, which affects the relative width of the feature; and the argument of periastron which affects the symmetry of the feature. The magnitude of the heartbeat feature is dependent on the radii of the components, their masses and gravity darkening exponents, and the orbital inclination.

To study the binary properties of KIC 5006817, we simultaneously modelled the photometric and radial velocity data of KIC 5006817 using the modelling code, PHOEBE (Prša & Zwitter 2005). This code is an extension of the Wilson-Devinney code (Wilson & Devinney 1971; Wilson 1979; Wilson & Van Hamme 2004) and combines the complete treatment of the Roche

potential with a detailed treatment of surface and horizon effects such as limb darkening, gravity darkening, ellipsoidal modulation and reflection effects to arrive at a comprehensive set of stellar and orbital parameters.

The orbital period of the binary is close to the length of one *Kepler* quarter (~3 months), which is the typical time scale of long term instrumental trends in *Kepler* data. Consequently, in the case of KIC 5006817, accurate detrending of the light curve is a challenge. We have therefore manually extracted each light curve, on a quarter-by-quarter basis, from pixel level data to create the best behaved light curve possible. We then fitted and divided out a linear trend from each Quarter to detrend and normalise the data. We selected a linear trend to avoid removing the beaming information from the light curve.

6.1. Orbital ephemeris

From the long cadence *Kepler* photometry of KIC 5006817 (Quarters 0–12) we determined the zero point in the data (the time of the periastron minimum) to be $2\,455\,019.221 \pm 0.008$ using the KEPHEM software package (Prša et al. 2011). Combining this with the spectroscopically determined period (94.812 ± 0.002 d) we obtained the following ephemeris in the Barycentric Julian date:

$$\text{Min } I = 2\,455\,019.221 \pm 0.008 + 94.812 \pm 0.002\,\text{d} \times E,$$

where E is the number of orbits.

6.2. Input parameters

In our fits, we have fixed the effective temperature of the primary component to the spectroscopic value: $T_{\text{eff,1}} = 5000$ K (Table 5).

Assuming the secondary component is a main sequence star (from its lack of visibility in the spectra), we can place an upper limit of ~5400 K on its effective temperature by assuming that it contributes 1 per cent of the total flux (the lower limit for spectral disentangling). This temperature is an upper limit and is likely an overestimate, given the mass determined from the binary model (~0.3 $M_\odot$, see Sect. 6.5 and Table 6). Due to the evolutionary state of the primary and low mass of the secondary, we assumed that both components have substantial convective outer envelopes and consequently adopted the standard albedo value of 0.6 (Ruciński 1969a,b). As both objects radiate towards the infrared end of the optical spectrum, as suggested by Diaz-Cordoves & Gimenez (1992) and van Hamme (1993), we have selected the square-root limb darkening law (Eq. (6) in Diaz-Cordoves & Gimenez 1992).

6.3. Fitting procedure

After manually tweaking the initial parameters until an approximate fit to the photometric data and the spectroscopic radial velocities was accomplished, we applied differential corrections (Wilson & Sofia 1976) to optimise the parameters.

The binary model created has the mass and radius of the primary component fixed to the asteroseismic value. Using differential corrections we simultaneously fitted the eccentricity and argument of periastron to the radil velocity and light curves; fitted the semi-major axis and gamma velocity to the radial velocity curve and fitted only the remaining parameters to the light curve. The fitted and fixed parameters of the best-fit model are listed in Table 6, Figs. 9 and 10 show the phase binned light curve and radial velocity data with the best-fit model (red line)
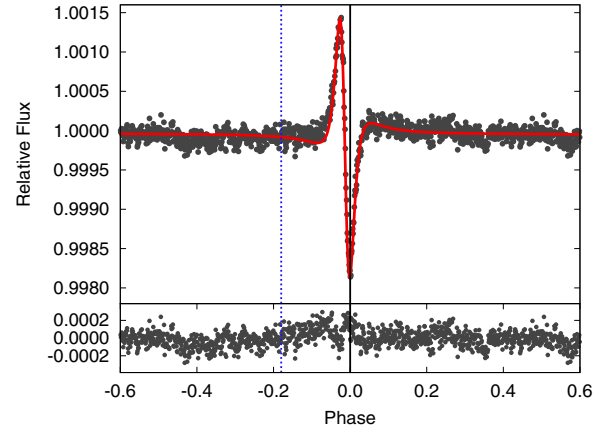

Fig. 10. Theoretical PHOEBE model without beaming (red line) and observed light curve (black points) of the phased (94.82 d), binned *Kepler* long-cadence data of Quarters 0–12. *Lower panel*: residuals of the best-fit model. The dashed and solid lines are centred on the times of superior and inferior conjunction respectively.

Table 6. Parameters and coefficients for the PHOEBE best-fit model to the *Kepler* light curve for Quarters 0–12 long cadence data for the non-beaming and beaming cases.

Parameter	Non-beaming	Beaming
Mass ratio, q	0.199 ± 0.001	0.20 ± 0.03
Secondary mass ($M_\odot$), M_2	0.30 ± 0.01	0.29 ± 0.03
Semi-major axis ($R_\odot$), a	106.1 ± 0.5	105.6 ± 0.9
Orbital eccentricity, e	0.71 ± 0.01	0.71 ± 0.02
Argument of periastron (rad), ω	4.0 ± 0.1	4.01 ± 0.06
Orbital inclination (°), i	62 ± 4	61 ± 6
Primary potential, Ω_1	16.7 ± 0.2	16.2 ± 0.2
Gamma velocity (km s^{-1}), γ	-14.01 ± 0.01	-14.43 ± 0.08
Primary $\log g$ (cgs), $\log g_1$	3.078 ± 0.007	3.022 ± 0.007
Gravity darkening exponent, GRD	1.00 ± 0.03	1.07 ± 0.03
Primary fractional point radius	0.0644	0.0679
Primary fractional pole radius	0.0637	0.0676
Phase of periastron	0.0121	0.0094
Primary x_1 coeff.	0.718	0.717
Primary y_1 coeff.	0.716	0.714
Fixed Parameters	Values: both Cases	
Primary T_{eff} (K)	5000 ± 250	
Third light	0.0	
Orbital period (d)	94.812 ± 0.002	
Time of primary minimum (BJD)	$245\,019.221 \pm 0.008$	
Primary bolometric albedo	0.6	

Notes. The secondary component's potential, radius and $\log g$ are not noted as these parameters have no signature in the light curve and radial velocity data. The fractional radii quoted are the radii relative to the semi-major axis. For the mass and radius of the primary component, see Table 1. The limb darkening coefficients (x_1 and y_1) are for the square root limb darkening law and were taken from the PHOEBE limb darkening tables (Prša et al. 2011). For the beaming case we assumed 100% of the flux comes from the primary component.

in the upper panel and the corresponding residuals in the lower panel.

6.4. The puzzling absence of a Doppler beaming signal

So far, we have not taken into account the effect of Doppler beaming on the light curve. Doppler beaming is caused by the radial velocity of the two stars and is the combined effect of shifting the stars' spectral energy distributions with respect to
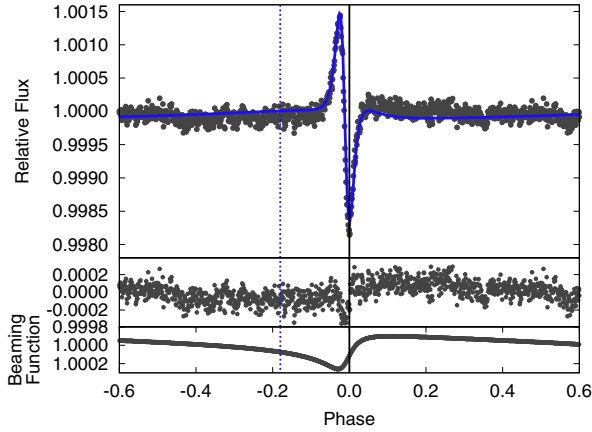
Fig. 11. Theoretical PHOEBE model similar to Fig. 10, but including beaming (blue line). The dotted and dashed lines are centred on the times of superior and inferior conjunction, respectively. *Middle panel*: residuals of the best-fit beaming model. *Lower panel*: Doppler beaming function that has been added to the model to incorporate beaming. The axis is inverted for comparison with the residuals.

the *Kepler* bandpass, aberration and an altered photon arrival rate. The net result of Doppler beaming is an increase in the observed flux from a star when it moves towards the observer, and a decrease when it moves away from the observer. It was predicted to be seen in *Kepler* data by Loeb & Gaudi (2003) and Zucker et al. (2007), and has recently been observed in several systems from ground-based data as well as *Kepler* and CoRoT light curves (see e.g. Mazeh & Faigler 2010; van Kerkwijk et al. 2010; Shporer et al. 2010; Bloemen et al. 2011).

Based on the radial velocity measurements of the primary star (semi-amplitude, $K = 11.78$ kms^{-1} – see Table 3), we estimate that Doppler beaming should have a significant contribution in the light from the red giant in KIC 5006817, of the order of $\sim$300 ppm. Since spectroscopy indicates that the secondary component in the binary has an insignificant luminosity compared to the primary, we looked into the effect of Doppler beaming assuming that all the observed flux is emitted by the red giant primary component. The Doppler beaming signal was modelled following Eq. (2) in Bloemen et al. (2011). The Doppler beaming coefficient of the red giant primary, which takes into account the spectrum of the star and the wavelength of the observations, was computed using Eq. (3) of Bloemen et al. (2011) to be $\langle B_1 \rangle = 4.59 \pm 0.21$ from Kurucz 2004 model spectra (Castelli & Kurucz 2004).

Figure 11 depicts the phase-folded light curve and best-fit model including beaming for KIC 5006817. The residuals of this model, however, contain a significant sinusoidal wave, similar in nature to that of the beaming function. The beaming signal thus seems to be invisible in the observed light curve. At phase zero the beaming signal has been fitted by adjusting the inclination of the model, however, the fit is still less adequate in this region than for the non-beaming case.

Possible reasons for the absence of a beaming signal in the data are a very high third light contamination which reduces the observed amplitude of the effect; a significant beaming signal from the secondary that partly or fully cancels out the beaming signal of the primary; or that the inherent long period instrumental trends in the *Kepler* data are concealing the beaming signal. The first possibility can be ruled out, since no bright source of third light is seen close to the target and no contaminating light was found in the spectra. To evaluate the second possibility –
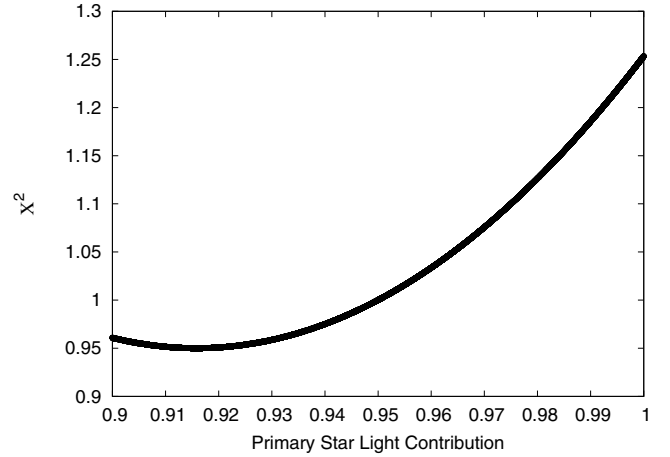
Fig. 12. The χ^2 goodness of fit to the continuum light curve (light curve with the periastron variation removed) as a function of the fraction of light contributed by the primary component, for multiple models. For each model the fraction of light was randomised (90–100 per cent for the primary component) and the beaming function was calculated for both the primary and secondary components. The goodness of fit was then assessed away from the periastron variation as only the beaming has an effect on this section of the light curve.
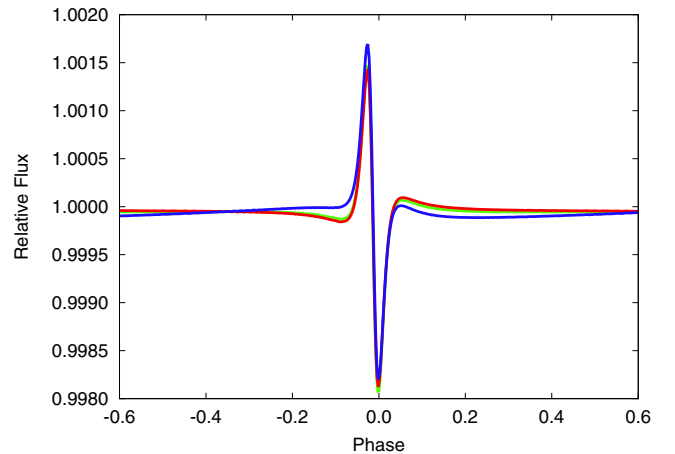

Fig. 13. Best-fit model to the phased light curve data (red), the same model with beaming and 100 per cent light contribution from the primary component (blue), and with beaming and 91.5 per cent light contribution from the primary component (green) – the best fit model when allowing the flux ratio to be fitted.

the beaming signal from the secondary is cancelling out the primary beaming signal, we scanned the parameter space to find the light ratio (with beaming from both components) that best fitted the data. We only fitted the continuum section of the light curve, since the beaming effect can be compensated for at the phase of the periastron variation by adjusting the inclination. When including Doppler beaming for the secondary component, we assumed that it is a main sequence object with a mass of 0.3 $M_\odot$, giving a Doppler beaming coefficient of $\langle B_2 \rangle \simeq 6.5$.

Figure 12 shows the χ^2 value as a function of primary light contribution. We find a clear preference for a contribution of 91.5 per cent from the primary component and 8.5 per cent from the secondary component. As shown in Fig. 13, the modelled light curve for the preferred light ratio (green line) is approximately equal to the light curve excluding beaming, suggesting that the preferred configuration leads to the secondary essentially cancelling out the beaming from the primary component. If the

secondary is a 0.3 $M_\odot$ main sequence star, it can not, however, contribute on the order of 8 per cent of the light in the system, and furthermore, a main sequence star this bright would have been easily detected in our spectroscopic data. We also considered the option that the secondary is a continuum white dwarf as this would not necessarily show up in the spectra. However, we can rule out this possibility as the temperature would need to be greater than 40 000 K for it to contribute 8.5 per cent of the flux and as such the light curve would show an extreme reflection effect (the white dwarf reflecting off the red giant), which we do not observe. We would also see evidence for such a white dwarf in the spectroscopic data, as continuum white dwarfs (which do not have a signal in spectroscopic data) have effective temperatures $\lesssim$12 000 K. Furthermore, a hot star would have a lower beaming factor and thus require a greater flux contribution from the secondary component.

Other than missing or incomplete physics in the binary models, the final possibility that we have postulated is that the *Kepler* satellite is not stable enough on longer timescales to preserve the beaming signal in the data. While this seems like a more convincing option, given that the trends in the *Kepler* light curves have a larger amplitude than the beaming signal, and that the timescales of the orbital period and a *Kepler* quarter are similar, we find it surprising that we are unable to detect any signature of the beaming signal given that we used a minimally evasive detrending method. We also note that the beaming signal was still missing when using a higher order Legendre polynomial in place of the linear trend.

The slope of the beaming signal is largest at the phase of the periastron brightening, and therefore significantly influences the optimal set of parameters found when fitting the heartbeat. Since we do not understand the absence of the beaming signal, we present the results of the fits to the data both including beaming, assuming 100 per cent light contribution from the primary, and without beaming. The optimal parameter values for both cases are listed in Table 6.

6.5. Mass ratio, primary potential and gravity darkening degeneracies

When fitting the binary characteristics, we found that the mass ratio, primary potential (which is essentially the inverse of the primary radius) and gravity darkening exponent are degenerate with each other. To assess the level of degeneracy between the potential and the gravity darkening exponent, a scan of the parameter space was undertaken whereby the primary gravity darkening exponent was randomly adjusted following which the primary potential and light factor were fitted to the light curve using differential corrections. Figure 14 shows the gravity darkening value and corresponding potentials for multiple models. The points are coloured with respect to their χ^2 value to show the goodness of fit for each individual model. The results show a complete degeneracy between the primary potential and primary gravity darkening exponent. Repeating this experiment for the primary potential and mass ratio, we again found a complete degeneracy. For this reason we elected to fix the primary mass and radius to the asteroseismically determined values, 1.49 ± 0.06 $M_\odot$ and 5.84 ± 0.08 $R_\odot$, respectively.

Keeping the gravity darkening exponent as a free parameter, we found a best binary model fit to the gravity darkening coefficient to be 1.00 ± 0.03 and 1.07 ± 0.03 for the beaming and non-beaming cases, respectively. These values are not in agreement with the accepted value of $GRD = 0.32$ for a star with a convective envelope (Lucy 1967), although this is an empirically
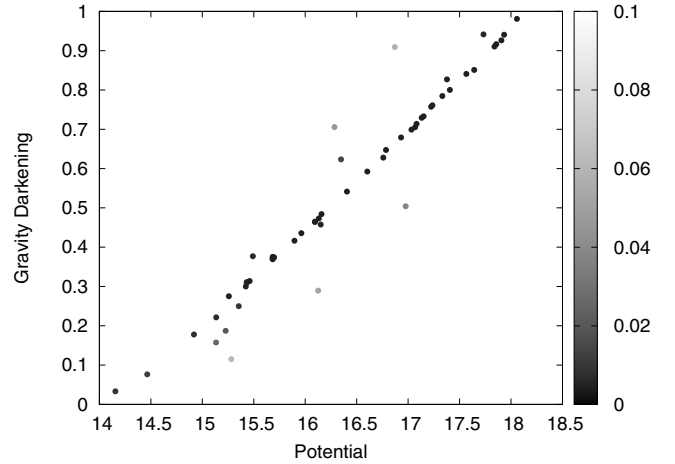

Fig. 14. Gravity darkening value as a function of the primary potential, where each point represents an individual binary model. For each model the gravity darkening exponent was determined randomly (between 0.0 and 1.0) and a model generated by fitting the light factor and potential, whilst keeping all other parameters fixed. The points are coloured by the χ^2 goodness of fit to demonstrate that the outliers are a consequence of an inadequate fit (the lower χ^2 values denote the better models, here depicted in black).

determined value for main sequence objects. More recent literature suggests an increased value of ~0.5 based on computations of atmosphere models (Claret & Bloemen 2011). In this case the value is specific for stars with an effective temperature and surface gravity close to that of the red giant in KIC 5006817. While this value is closer to that determined, there is still a large discrepancy between the observed and theoretical values. A possibility is that the uncertainties of the asteroseismic mass and radius are underestimated. However, a closer look suggests that the radius would have to increase by three sigma and the mass decrease by three sigma to reach the gravity darkening exponent suggested by Claret & Bloemen (2011). While a three sigma limit may be plausible, the change in values would require the density – the most constrained asteroseismic value – to deviate significantly from that determined, which is unlikely. The most likely explanation is that the accepted gravity darkening exponent needs to be revised or completely mitigated from the models (Espinosa Lara & Rieutord 2012).

6.6. Uncertainty determination

The uncertainties of the parameters were determined using two methods: through standard errors and their propagation, and through Monte Carlo heuristic scanning. A scan of the parameter space was undertaken for the most correlated (but not completely degenerate) parameters, which were determined by applying the correlation matrix function in PHOEBE. With a fixed mass ratio and gravity darkening, the most correlated parameters were determined to be the inclination, eccentricity and argument of periastron. The magnitude of the periastron brightening was not found to be significantly correlated with these parameters, which determine the shape of the periastron brightening.

We applied Monte Carlo simulations to perturb the solutions of the eccentricity, argument of periastron and inclination. The applied method required the computation of the potential and phase shift, and the iterative randomisation of the eccentricity and argument of periastron by 10 per cent, and the inclination by 20 per cent. At each iteration a comparison between
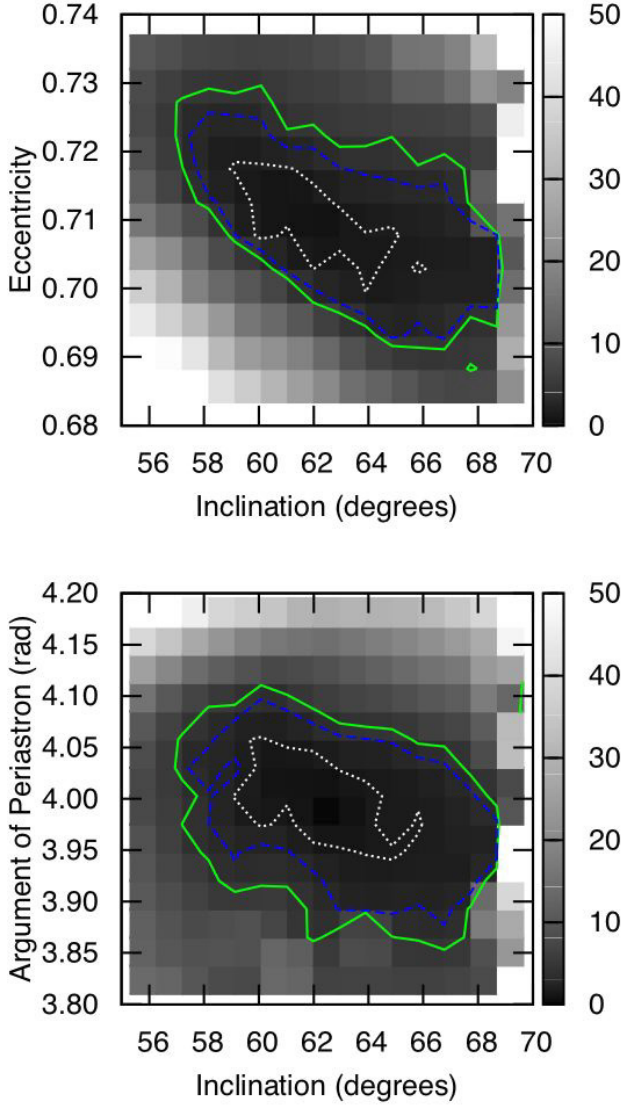
Fig. 15. Density maps of the Monte Carlo simulations of the inclination vs. eccentricity (*upper panel*) and the inclination vs. argument of periastron (*lower panel*) for the non-beaming case. The grey scale depicts the χ^2 values mapped across the grid. The colour bar depicts the grey scale pertaining to the different values of χ^2. The contours (from inner to outer) denote the 1σ (dotted white line), 2σ (dashed blue line) and 3σ (solid green line) confidence intervals. The uncertainties for the inclination, argument of periastron and eccentricity were determined using the 1σ confidence contours displayed.

the model and phased data was made using the χ^2 statistical test. The χ^2 values for each solution were then mapped out across a parameter grid with confidence intervals, which serve as uncertainty estimates (cf. Fig. 15). The optimum combination of the displayed parameters can be identified from the density maps, where the 1σ, 2σ and 3σ uncertainty values are presented as contours.

7. Combined asteroseismic and binary interpretation

Assuming the equilibrium tide model (Zahn 1966, 1989; Remus et al. 2012), which applies to stars with convective outer envelopes, we calculated approximate timescales for the synchronisation and circularisation of KIC 5006817, using the work of
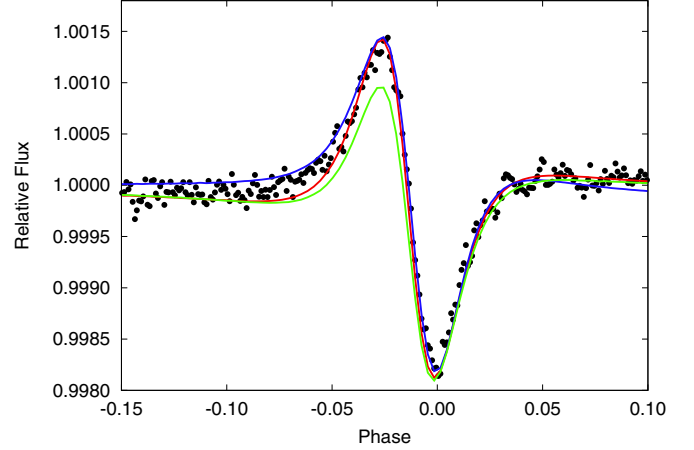
Fig. 16. Comparison between the data (grey points), the best-fit light curve model without beaming (dotted red line), the best-fit model with beaming (dashed blue line), and the best-fit model for an imposed orbital inclination of 76°, as determined through asteroseismology (solid green line). A change in the inclination changes the ratio between the maximum and minimum of the periastron variation (also known as the heartbeat event).

Zahn (1977). The synchronisation timescale denotes the amount of time needed for the star's rotational angular velocity to equal its orbital angular velocity at periastron (pseudo-synchronous rotation) and for the stars' axes to become perpendicular to the orbit. The circularisation time scale is the maximum time the orbit will take to circularise. Applying Eq. (6.1) of Zahn (1977) we determined the synchronisation timescale due to gravitational interactions to be 2×10^{12} yr, which is prohibitively large.

To determine whether KIC 5006817 is synchronised we compared the inclination of the orbit and the rotational axis, and considered the rotation rate of the red giant. The inclination measured from rotational splitting is sensitive to the orientation of the rotational axis of the primary pulsator, while the inclination determined from the shape of the heartbeat event describes the orientation of the orbital plane. In the case of KIC 5006817, these two inclination angles were found to agree within 2σ: $i_{rot} = 77° \pm 9°$ versus $i_{orbit} = 62° \pm 4°$ (61° ± 6° for the beaming case).

To assess this difference graphically, Fig. 16 compares the best-fit binary model without beaming (red) and with beaming (blue) and with the orbital model with an imposed orbital inclinations of 76° (green) taken from asteroseismology. It is clear that the maximum in the light curve is not well approximated with such a high orbital inclination. On the other hand, the very low visibility of the zonal modes ($|m| = 0$) in the centre of the rotationally split triplets, under the assumption of equal intrinsic amplitudes, definitely excludes inclinations below 70°.

If the system were rotating pseudo-synchronously, following Eq. (44) of Hut (1981), using the observationally derived eccentricity and orbital period, one would expect a rotation period of about 11 d for KIC 5006817. Such rapid surface rotation is immediately ruled out from the width of the absorption lines in the spectrum of the primary. Moreover, the splitting of the $l = 1$ modes points towards a rotation period of at least 165 d, which is more than 1.7 times the orbital period. Thus we conclude that, as expected, KIC 5006817 is not in a synchronised orbit.
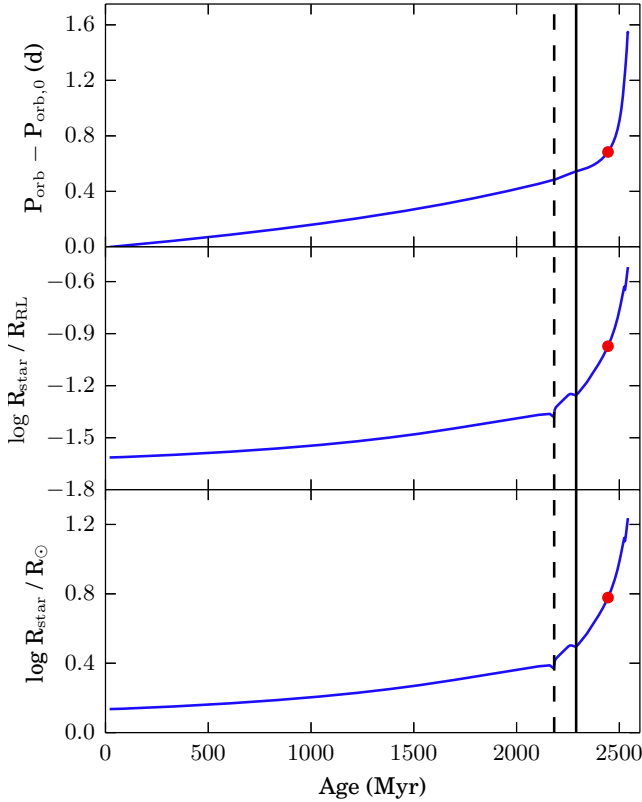
Fig. 17. Modelling the orbital period (*top panel*), Roche lobe filling factor (*middle panel*) and radius of the red giant main component (*lower panel*) of binary system with MESA with the approximated values of KIC 5006817. The models start at the zero age main sequence (ZAMS) and stop with the onset of the RLOF. The dashed line marks the end of the hydrogen core burning (TAMS). The solid line marks the bottom of the RGB. The position of a model with the radius of $6\,R_{\odot}$, which equals the current state of KIC 5006817 is shown as a red dot.

8. Impact of stellar evolution on eccentric binary systems

Most hot subdwarf B (sdB) stars and cataclysmic variables (CV) are supposed to be produced from binaries that have undergone mass transfer and drastic mass loss during either a common envelope (CE) phase or a phase of stable Roche lobe overflow while on the RGB (Han et al. 2002, 2003; Nelemans & Tout 2005). Several unsolved questions remain regarding the exact sdB-progenitors and the details of the mass loss mechanism (Hu et al. 2008; Østensen 2009; Heber 2009).

8.1. Modelling the binary evolution of KIC 5006817

Currently, the binary system KIC 5006817 is dynamically stable on timescales shorter than the evolutionary timescales of the red giant component. The system parameters, determined in the previous sections show that in its current configuration the orbit is wide compared to the Roche radii of the components. The low mass of the secondary component suggests that this star is most likely an M dwarf, which will stay on the main sequence for the remaining lifetime of the red giant companion. The evolution of the system will therefore mainly depend on the evolution of the red giant component (Fig. 17).

MESA[1] (Paxton et al. 2010, 2011, 2013) is a one dimensional stellar evolution code originally designed for single star evolution. The code is adapted to handle binary systems by letting them evolve one step at a time, after which the orbital evolution is updated as well. The standard binary evolution that is included in MESA (version: November 2012) only handles the evolution of circular binaries. To check the evolution of an eccentric binary in which one of the components is a red giant, we implemented the equations derived by Verbunt & Phinney (1995) to account for tidal interactions. The evolution of the eccentricity is governed by,

$$\frac{\mathrm{d}\ln e}{\mathrm{d}t} = -1.7 f \left(\frac{T_{\mathrm{eff}}}{4500\,\mathrm{K}}\right)^{\frac{4}{3}} \left(\frac{M_{\mathrm{env}}}{M_{\odot}}\right)^{\frac{2}{3}} \frac{M_{\odot}}{M} \frac{M_2}{M} \frac{M + M_2}{M} \left(\frac{R}{a}\right)^{8} \frac{1}{\mathrm{yr}}$$

(5)

where M_{env} is the mass of the convective envelope of the RG star. M_2 is the mass of the companion and a refers the semi-major axis of the orbit. The factor f is calculated based on the mixing length parameter α,

$$f = 1.01 \left(\frac{\alpha}{2}\right)^{(4/3)}.$$

(6)

At every time step of MESA, M_{env} and T_{eff} are obtained from the stellar structure model. The start of the Roche lobe overflow (RLOF) is calculated based on the Roche-Lobe calculated at periastron passage.

To study the changes of eccentricity, period and the radius of the Roche lobe on such an eccentric binary system caused by the red giant evolution, we created an approximate model of the system KIC 5006817, using the starting masses $M_{\mathrm{RG}} = 1.5\,M_{\odot}$ and $M_{\mathrm{MS}} = 0.3\,M_{\odot}$, an initial orbital period $P_{\mathrm{orbit},0} = 94.0\,\mathrm{d}$ and eccentricity to $e = 0.70$. On the red giant branch a Reimers wind (Kudritzki & Reimers 1978) was assumed, with $\eta = 0.5$.

When we let this binary model evolve, we find that the orbital period slowly increases during the main sequence evolution (Fig. 17, top panel); the rate of increase will accelerate as the star starts to ascend the red giant branch, mainly caused by mass loss due to the stellar wind on the RGB (Hurley et al. 2002). The eccentricity remains stable. Only when the red giant is close to filling its Roche lobe, the system will circularise on the order of a few 10 000 years.

The middle panel of Fig. 17 depicts how the expanding radius of the red giant component gradually grows to fill its Roche lobe ($R_{\mathrm{star}}/R_{\mathrm{Roche\,Lobe}} < 1$). From the bottom panel of Fig. 17, it becomes obvious that the onset of RLOF at periastron passages will happen well below the tip of the RGB. From MESA single models, we find that a giant of $1.5\,M_{\odot}$ will have a maximum radius of about $140\,R_{\odot}$ before igniting helium. Exactly how the orbital period will change during this process depends on how much of the transferred mass is accreted by the companion, and how much escapes the system.

The periastron distance is $32 \pm 1\,R_{\odot}$, which corresponds to $\sim$4 times the current radius of the red giant. When exceeding a radius, larger than the current semi-major axis of $106\,R_{\odot}$ (Table 6), the red giant will completely engulf its companion in all phases of the orbit, leading to a CE phase while it is ascending the RGB. The interaction between two components during the CE phase for a rather similar system has been studied by Han et al. (2002), showing that the secondary component

---

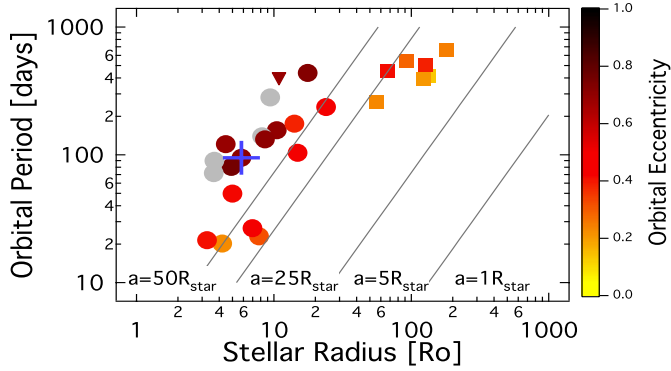[1] Modules for Experiments in Stellar Astrophysics, see http://mesa.sourceforge.net

Fig. 18. Stellar radius of the main component versus the orbital period of the binary system. Colour indicates the eccentricity of the systems (Table 3). Stars from our sample (Tables 1 and 2) are plotted as filled dots. KIC 5006817 is marked with a cross. The eclipsing red giant KIC 8410637 (Hekker et al. 2010; Frandsen et al. 2013) is shown as a triangle. The stars found in the LMC (Nicholls & Wood 2012) are shown as squares. Solid lines show the period of a system with a total mass of 1.8 $M_\odot$ and a semi-major axis, which is a multiple of the stellar radius.

Fig. 19. Comparing the eccentricities of known eccentric systems with ellipsoidal modulation. Colour indicates the $\log g$ of the red giant component. Dots represent the stars from our sample for which we could derive the eccentricities from radial velocities. KIC 5006817 and KIC 8410637 are shown as a cross and triangle, respectively. Squares show the derived eccentricities of the stars in the LMC.

will spiral down inside the red giant primary. This phase happens rapidly compared to the evolutionary time scale of the red giant. A critical point is reached when the companion arrives at the bottom of the convective envelope and penetrates the initially radiative zone below it. The dynamical instability that follows will eject the envelope unless the companion is disrupted first (Han et al. 2002).

Once the red giant ejects its envelope, we are left with the "naked" stellar core. If the red giant enters a CE-phase near the tip of the RGB, we would find a helium core which will become sdB stars. Otherwise, the system is likely to become a CV. Currently a majority of the observed long period sdB binaries have an eccentric orbit (Vos et al. 2013), indicating that their progenitor must have had a high eccentricity as well, as is the case with hearthbeat stars. We therefore expect to find nearly exclusively stars in the H-shell burning phase in these eccentric systems and hardly any stars which have experienced He-core ignition and now settled on the red clump. The latter is only expected if the system's separation is large enough.

8.2. Comparison to other known red giant stars in eccentric binary systems

As a consequence of the expanding radius of the red giant, a relation between the radius of the primary and the orbital period for such interacting systems is expected, since only binaries with large enough periastron distances can stably exist. From seismology, we obtained the radii of a sample of red giant stars, located in such eccentric systems that are undergoing gravitational distortion, to a range between 2 and 24 $R_\odot$, as given in Table 1. Nicholls & Wood (2012) reported seven similar systems from OGLE observations of the Large Magellanic Cloud (LMC). Although the OGLE light curves are not suitable for seismic investigations, they can constrain the fundamental parameters of the stars from modelling the phase diagram and photometric calibrations. The red giant systems found in the LMC are higher up in the HR Diagram than the stars in our sample and also have in general longer orbital periods (260−660 d). Figure 18, in which the stellar radii and orbital periods of the stars in the LMC and *Kepler* sample are compared, shows that systems hosting bigger
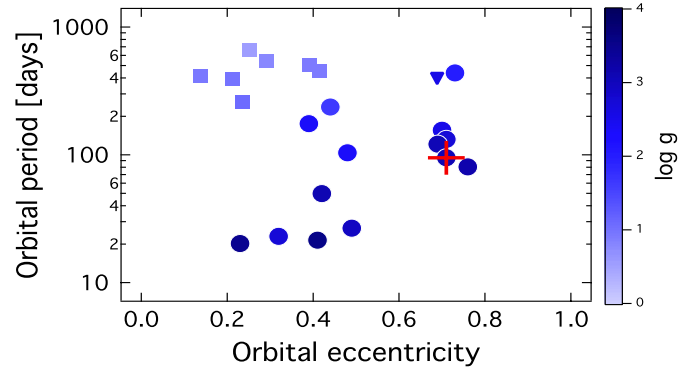
stars tend to have longer periods and ellipsoidal variation occurs for a specific combination of stellar radius and orbital period. We note that our sample is biased due to the selection of stars which show the heartbeat effect. However, as shorter periods lead to smaller systems, which cannot stay stable for a long time. These stars show a minimum orbital periods. In systems with shorter period mass transfer should eventually occur.

In our ongoing spectroscopic campaign we have currently obtained enough radial velocity measurements for 14 systems in our sample to derive their orbital parameters. The full orbital parameters of these systems are given in Table 3. Fig. 19 depicts the eccentricities of the red giant heartbeat stars on the lower RGB found with *Kepler* from our sample with the eccentricities of those close to the tip of the RGB (Nicholls & Wood 2012). The majority of the systems in Table 1 for which we have RV data have eccentricities between $0.23 < e < 0.5$, which is compatible with the range of eccentricities reported by Thompson et al. (2012) for their objects. Also, the 4 stars with periods shorter than 30 d belong to the least eccentric in our sample. Among the long periodic systems, 5 exhibit eccentricities larger than 0.7. Our most eccentric system is KIC 8144355 ($P_{\rm Orbit} = 80.6$ d, $e = 0.76 \pm 0.01$).

The systems found in the LMC so far have eccentricities that range between $0.15 < e < 0.45$, which suggests that the stars might have experienced some circularisation. It is not yet clear if mass transfer has already started in these systems or if the circularisation is forced by tidal interaction. Yet the two samples are too small to draw a firm conclusion. In subsequent work, we will further investigate the distribution of eccentricities in the *Kepler* red giant heartbeat stars from photometric and radial velocity data on larger datasets.

Finally, we note that KIC 8410637, an eclipsing binary with a 408 d period (Hekker et al. 2010; Frandsen et al. 2013) has a period and a high eccentricity ($e \sim 0.7$), compatible with the other red giant heartbeat stars (Figs. 18 & 19) but no heartbeat events are visible.

9. Conclusions

In this work we have studied a sample of 18 red giant stars in eccentric binary systems, detected with the *Kepler* satellite, that exhibit flux modulation as a result of binary interaction during their periastron passage. All giants in the systems in our sample

exhibit solar-like oscillations, so we applied asteroseismic techniques to determine their global properties, as well as their evolutionary states. As shown in the analysis of one selected system, the approach of combining asteroseismic and binary modelling analyses is very powerful.

For KIC 5006817, this new approach revealed a low mass companion with a mass of $M_2 = 0.29 \pm 0.03 \ M_\odot$ (where the uncertainty encompasses both the beaming and non-beaming cases). Estimates based on the radial velocity curve and the optical spectrum revealed that Doppler beaming should be contributing 300 ppm to the light curve although the light curve modelling did not support this. This is possibly a consequence the long term trends in the *Kepler* data, given that the period of KIC 5006817 is ~95 d, which is very close to the length of a *Kepler* quarter (90 d).

Through modelling the binary characteristics, while fixing the primary mass and radius to the asteroseismically determined values, the gravity darkening value was determined to be $GRD = 1.0 \pm 0.03$ for the non-beaming case and $GRD = 1.07 \pm 0.03$ for the beaming case. These values are inconsistent with the empirical value determined by Lucy (1967), $GRD = 0.32$, and the more recent model dependent value determined by Claret & Bloemen (2011), $GRD = 0.5$. To obtain a binary model with values closer to those predicted by theory, the density of the primary component would need to deviate significantly from the well constrained asteroseismic value. For this reason we speculate that the gravity darkening values require further revision.

From modelling the binary evolution of an approximate binary system, we conclude that the system is in fact too young to be synchronised. When comparing the properties of the full sample (Table 1), we found a correlation between the radius of the primary red giant component and the orbital period. Furthermore, all stars show seismic characteristics of stars in the state of H-shell burning. For a few, we cannot rule out a membership of the red clump or AGB. We argue that this is an effect of stellar evolution as the red giant's radius along the red giant branch will increase until the helium core ignites. If a system gets too close, it can undergo a common envelope phase which could lead to the ejection of the convective envelope of the red giant. This scenario is a potential evolutionary channel for the formation of cataclysmic variables and sdB stars.

Our sample is an interesting class of ellipsoidal variables which offers unique conditions to study interactions in and the evolution of eccentric binary systems. Optimal cases are systems which show the heartbeat effect and exhibit primary and secondary eclipses or are double lined spectroscopic binaries, as for such systems also for the secondary component independent fundamental parameters can be derived. The ensemble of stars presented here allows us to study the binary interaction and the future fate of such eccentric systems in a new way, to help unravel common-envelope physics.

References

Ballot, J., García, R. A., & Lambert, P. 2006, MNRAS, 369, 1281
Beck, P. G., Bedding, T. R., Mosser, B., et al. 2011, Science, 332, 205
Beck, P. G., Montalban, J., Kallinger, T., et al. 2012, Nature, 481, 55
Bedding, T. R., Mosser, B., Huber, D., et al. 2011, Nature, 471, 608
Bildsten, L., Paxton, B., Moore, K., & Macias, P. J. 2012, ApJ, 744, L6
Bloemen, S. 2013, Ph.D. Thesis, University of Leuven, Belgium
Bloemen, S., Marsh, T. R., Østensen, R. H., & et al. 2011, MNRAS, 410, 1787
Borucki, W. J., Koch, D., Basri, G., et al. 2010, Science, 327, 977
Castelli, F., & Kurucz, R. L. 2004, IAU Symp., 210, poster A20
Christensen-Dalsgaard, J., Schou, J., & Thompson, M. J. 1990, MNRAS, 242, 353
Claret, A., & Bloemen, S. 2011, A&A, 529, A75
Corsaro, E., Fröhlich, H.-E., Bonanno, A., et al. 2013, MNRAS, 430, 2313
De Ridder, J., Barban, C., Carrier, F., et al. 2006, A&A, 448, 689
De Ridder, J., Barban, C., Baudin, F., et al. 2009, Nature, 459, 398
De Smedt, K., Van Winckel, H., Karakas, A. I., et al. 2012, A&A, 541, A67
Deheuvels, S., García, R. A., Chaplin, W. J., et al. 2012, ApJ, 756, 19
Demarque, P., Guenther, D. B., Li, L. H., Mazumdar, A., & Straka, C. W. 2008, ApSS, 316, 31
Diaz-Cordoves, J., & Gimenez, A. 1992, A&A, 259, 227
Donati, J.-F., Semel, M., Carter, B. D., Rees, D. E., & Collier Cameron, A. 1997, MNRAS, 291, 658
Dupret, M.-A., Belkacem, K., Samadi, R., et al. 2009, A&A, 506, 57
Espinosa Lara, F., & Rieutord, M. 2012, A&A, 547, A32
Feroz, F., Hobson, M. P., & Bridges, M. 2009, MNRAS, 398, 1601
Frandsen, S., Carrier, F., Aerts, C., et al. 2002, A&A, 394, L5
Frandsen, S., Lehmann, H., Hekker, S., et al. 2013, A&A, 556, A138
García, R. A., Hekker, S., Stello, D., et al. 2011, MNRAS, 414, L6
Gaulme, P., McKeever, J., Rawls, M. L., et al. 2013, ApJ, 767, 82
Gizon, L., & Solanki, S. K. 2003, ApJ, 589, 1009
Goupil, M. J., Mosser, B., Marques, J. P., et al. 2013, A&A, 549, A75
Grevesse, N., Noels, A., & Sauval, A. J. 1996, in Cosmic Abundances, eds. S. S. Holt, & G. Sonneborn, ASP Conf. Ser., 99, 117
Guenther, D. B. 1994, ApJ, 422, 400
Guenther, D. B., Demarque, P., Kim, Y.-C., & Pinsonneault, M. H. 1992, ApJ, 387, 372
Hadrava, P. 1995, A&AS, 114, 393
Hambleton, K. M., Kurtz, D. W., Prša, A., et al. 2013, MNRAS, 434, 925
Han, Z., Podsiadlowski, P., Maxted, P. F. L., Marsh, T. R., & Ivanova, N. 2002, MNRAS, 336, 449
Han, Z., Podsiadlowski, P., Maxted, P. F. L., & Marsh, T. R. 2003, MNRAS, 341, 669
Heber, U. 2009, Ann. Rev. Astron. Astrophys., 47, 211
Hekker, S., Aerts, C., De Ridder, J., & Carrier, F. 2006, A&A, 458, 931
Hekker, S., Debosscher, J., Huber, D., et al. 2010, ApJ, 713, L187
Hekker, S., Elsworth, Y., De Ridder, J., et al. 2011, A&A, 525, A131
Hu, H., Dupret, M.-A., Aerts, C., et al. 2008, A&A, 490, 243
Huber, D., Bedding, T. R., Stello, D., et al. 2011, ApJ, 743, 143
Huber, D., Ireland, M. J., Bedding, T. R., et al. 2012, ApJ, 760, 32
Hurley, J. R., Tout, C. A., & Pols, O. R. 2002, MNRAS, 329, 897
Hut, P. 1981, A&A, 99, 126
Ilijic, S., Hensberge, H., Pavlovski, K., & Freyhammer, L. M. 2004, in Spectroscopically and Spatially Resolving the Components of the Close Binary Stars, eds. R. W. Hilditch, H. Hensberge, & K. Pavlovski, ASP Conf. Ser., 318, 111
Kallinger, T., Gruberbauer, M., Guenther, D. B., Fossati, L., & Weiss, W. W. 2010a, A&A, 510, A106
Kallinger, T., Mosser, B., Hekker, S., et al. 2010b, A&A, 522, A1
Kallinger, T., Hekker, S., Mosser, B., et al. 2012, A&A, 541, A51
Kjeldsen, H., & Bedding, T. R. 1995, A&A, 293, 87
Kochukhov, O., Makaganiuk, V., & Piskunov, N. 2010, A&A, 524, A5
Kudritzki, R. P., & Reimers, D. 1978, A&A, 70, 227
Kumar, P., Ao, C. O., & Quataert, E. J. 1995, ApJ, 449, 294

Kupka, F. G., Ryabchikova, T. A., Piskunov, N. E., Stempels, H. C., & Weiss, W. W. 2000, Baltic Astron., 9, 590

Ledoux, P. 1951, ApJ, 114, 373

Loeb, A., & Gaudi, B. S. 2003, ApJ, 588, L117

Lucy, L. B. 1967, ZAp, 65, 89

Matijevič, G., Prša, A., Orosz, J. A., et al. 2012, AJ, 143, 123

Mazeh, T., & Faigler, S. 2010, A&A, 521, L59

Mosser, B., Barban, C., Montalbán, J., et al. 2011a, A&A, 532, A86

Mosser, B., Belkacem, K., Goupil, M. J., et al. 2011b, A&A, 525, L9

Mosser, B., Goupil, M. J., Belkacem, K., et al. 2012a, A&A, 548, A10

Mosser, B., Goupil, M. J., Belkacem, K., et al. 2012b, A&A, 540, A143

Mosser, B., Michel, E., Belkacem, K., et al. 2013, A&A, 550, A126

Murphy, S. J., Shibahashi, H., & Kurtz, D. W. 2013, MNRAS, 430, 2986

Nelemans, G., & Tout, C. A. 2005, MNRAS, 356, 753

Nicholls, C. P., & Wood, P. R. 2012, MNRAS, 421, 2616

Østensen, R. H. 2009, Commun. Asteroseismol., 159, 75

Paxton, B., Bildsten, L., Dotter, A., et al. 2010, Astrophysics Source Code Library, ascl: 1010.083

Paxton, B., Bildsten, L., Dotter, A., et al. 2011, ApJS, 192, 3

Paxton, B., Cantiello, M., Arras, P., et al. 2013, ApJS, 208, 4

Prša, A., & Zwitter, T. 2005, ApJ, 628, 426

Prša, A., Batalha, N., Slawson, R. W., et al. 2011, AJ, 141, 83

Raskin, G., van Winckel, H., Hensberge, H., et al. 2011, A&A, 526, A69

Remus, F., Mathis, S., & Zahn, J.-P. 2012, A&A, 544, A132

Ruciński, S. M. 1969a, Acta Astron., 19, 125

Ruciński, S. M. 1969b, Acta Astron., 19, 245

Schou, J., Antia, H. M., Basu, S., et al. 1998, ApJ, 505, 390

Shporer, A., Kaplan, D. L., Steinfadt, J. D. R., et al. 2010, ApJ, 725, L200

Slawson, R. W., Prša, A., Welsh, W. F., et al. 2011, AJ, 142, 160

Sneden, C. A. 1973, Ph.D. Thesis, The Univerisity of Texas at Austin, USA

Stellingwerf, R. F. 1978, ApJ, 224, 953

Tassoul, M. 1980, ApJS, 43, 469

Thompson, S. E., Everett, M., Mullally, F., et al. 2012, ApJ, 753, 86

Tkachenko, A., Van Reeth, T., Tsymbal, V., et al. 2013, A&A, 560, A37

van Hamme, W. 1993, AJ, 106, 2096

van Kerkwijk, M. H., Rappaport, S. A., Breton, R. P., et al. 2010, ApJ, 715, 51

Verbunt, F., & Phinney, E. S. 1995, A&A, 296, 709

Vos, J., Østensen, R. H., Németh, P., et al. 2013, A&A, 559, A54

Welsh, W. F., Orosz, J. A., Aerts, C., et al. 2011, ApJS, 197, 4

Wilson, R. E. 1979, ApJ, 234, 1054

Wilson, R. E., & Devinney, E. J. 1971, ApJ, 166, 605

Wilson, R. E., & Sofia, S. 1976, ApJ, 203, 182

Wilson, R. E., & Van Hamme, W. 2004, Computing Binary Star Observables (in Reference Manual to the Wilson-Devinney Program)

Zahn, J. P. 1966, Ann. d'Astrophys., 29, 489

Zahn, J.-P. 1977, A&A, 57, 383

Zahn, J.-P. 1989, A&A, 220, 112

Zucker, S., Mazeh, T., & Alexander, T. 2007, ApJ, 670, 1326